Ultrasonics Sonochemistry 31 (2016) 610–625

Contents lists available at ScienceDirect

Ultrasonics Sonochemistry

journal homepage: www.elsevier.com/locate/ultson

Positional stability and radial dynamics of sonoluminescent bubbles under bi-harmonic driving: Effect of the high-frequency component and its relative phase

J.M. Rosselló [a,*,1], D. Dellavale [b,1], F.J. Bonetto [a]

[a] Laboratorio de Cavitación y Biotecnología, Instituto Balseiro-CONICET, Centro Atómico Bariloche, Río Negro, Argentina
[b] Laboratorio de Bajas Temperaturas, Instituto Balseiro-CONICET, Centro Atómico Bariloche, Río Negro, Argentina

ARTICLE INFO

Article history:
Received 2 January 2016
Received in revised form 5 February 2016
Accepted 9 February 2016
Available online 10 February 2016

Keywords:
Sonoluminescence (SBSL)
Bi-harmonic driving
Positional instability
Bjerknes force
Relative phase 78.60.Mq
43.25.Yw
43.35.Hl

ABSTRACT

The use of bi-frequency driving in sonoluminescence has proved to be an effective way to avoid the spatial instability (pseudo-orbits) developed by bubbles in systems with high viscous liquids like sulfuric or phosphoric acids. In this work, we present extensive experimental and numerical evidence in order to assess the effect of the high frequency component (P_{Ac}^{HF}) of a bi-harmonic acoustic pressure field on the dynamic of sonoluminescent bubbles in an aqueous solution of sulfuric acid. The present study is mainly focused on the role of the harmonic frequency (Nf_0) and the relative phase between the two frequency components (φ_b) of the acoustic field on the spatial, positional and diffusive stability of the bubbles. The results presented in this work were analyzed by means of three different approaches. First, we discussed some qualitative considerations about the changes observed in the radial dynamics, and the stability of similar bubbles under distinct bi-harmonic drivings. Later, we have investigated, through a series of numerical simulations, how the use of high frequency harmonic components of different order N, affects the positional stability of the SL bubbles. Furthermore, the influence of φ_b in their radius temporal evolution is systematically explored for harmonics ranging from the second to the fifteenth harmonic ($N = 2$–15). Finally, a multivariate analysis based on the covariance method is performed to study the dependences among the parameters characterizing the SL bubble. Both experimental and numerical results indicate that the impact of P_{Ac}^{HF} on the positional instability and the radial dynamics turns to be progressively negligible as the order of the high frequency harmonic component grows (i.e. $N \gg 1$), however its effectiveness on the reduction of the spatial instability remains unaltered or even improved.

1. Introduction

Sonoluminescence is a physical phenomenon characterized by the emission of light pulses from a gas bubble which is forced to have regular cycles of expansion and compression through the action of an sound wave. When the amplitude of the acoustic pressure field is slightly above the static pressure of the fluid (P_0) the bubble oscillatory regime become highly nonlinear. In this extreme situation the energy focused in the spherically converging inertial collapses is enough to produce a sudden rise in the pressure, density and gas temperature within the bubble. Consequently, a hot plasma core is produced from the gas and very short pulse of visible (and invisible) light is emitted (100 ps–2 ns of duration) [1]. In the cases where a stationary acoustic field is used, the sonoluminescent bubbles can be trapped and stabilized in the liquid medium for long periods of time (several hours or even days).

Single bubble sonoluminescence (SBSL) in a stable fashion was performed for the first time by Gaitan in 1992 [2], who trapped an air bubble in a mixture of glycerin and water using single frequency acoustic driving. A few years after the discovery of SBSL, researchers began to study the potential effects that the use of multi-frequency driving could have on the bubble dynamics [3–10]. Taking the single frequency case as a reference, some of the effects found on these studies can be summarized as follows: a variation in the emitted light intensity [3,7,11]; the high frequency components of the acoustic field (P_{Ac}^{HF}) promotes the generation of cavitation bubbles and avoid its dissolution [12]; an increment in the expansion rates of the bubbles R_{max}/R_0 [5,7,9]; P_{Ac}^{HF} can also affect the positional stability of the bubbles [4,5]. However, most of these studies were carried out using low viscosity liquids like water.

* Corresponding author.
[1] These authors contributed equally to this work.

http://dx.doi.org/10.1016/j.ultsonch.2016.02.013
1350-4177/

Many experimental and theoretical works have shown that when low viscosity liquids are used, the bubbles are susceptible to extinction by the bubble breakup that takes place due to the shape instabilities (Rayleigh–Taylor and Parametric) [13,14]. This motivated the realization of experiments using viscous fluids with low vapor pressure like sulfuric acid (H_2SO_4) or phosphoric acid (H_3PO_4) [15–17]. In this case, two other type of instabilities can occur, one is called *spatial* instability, while the other one is refereed as *positional* instability. The first one is characterized by the appearance of pseudo-orbits (around a fixed point) in the bubble trajectory [18]. In 2008 Urteaga and Bonetto [11] demonstrated that the combined use of a bi-harmonic driving was an effective way to remove the spatial instability. This result was recently confirmed and also extended in Refs. [19–22]. On the other hand, the positional instability occurs when the acoustic pressure amplitude applied to the bubble exceeds a limit value defined by the balance of the hydrodynamic forces affecting the bubble ($\vec{F}_b$), which is mainly determined by the Bjerknes primary force. Thus, when this frontier of maximum pressure is crossed (i.e. $P_{Ac}|_{\vec{F}_b=0}$) the net force applied on the bubble changes its sign, and as the equilibrium position is modified, the bubble is drifted away from the pressure antinode until a new position with an acoustic pressure similar to $P_{Ac}|_{\vec{F}_b=0}$ is reached and the force is once again balanced [23,24]. Furthermore, Dellavale et al. [19] have experimentally shown that biharmonic excitation is a mechanism that makes it possible to positionally (and spatially) stabilize SL bubbles in SA85 for very low dissolved gas concentrations, allowing to reach regions of parameter space were the intensity of the bubble collapse is upscaled.

The main advantage of using harmonic frequencies in the driving signal is to have a stationary acoustic field. The latter is the superposition of a low frequency component (P_{Ac}^{LF}) (with amplitude $P_{Ac}^{LF}|_0$ and a fundamental frequency f_0), and a high frequency component P_{Ac}^{HF} determined by its amplitude $P_{Ac}^{HF}|_0$, the harmonic order (N) and the relative phase between the P_{Ac}^{LF} and P_{Ac}^{HF} defined as φ_b.

It is already been established that φ_b can change either the position and the emitted light. A systematic investigation about the influence of φ_b on a SBSL fixed bubble in water under bi-harmonic driving, can be found for a case with $N = 2$ in Refs. [3,7,5,8–10]. It has also been stated that the equilibrium position reached by the bubbles is a direct consequence of the complex acoustic field structure and the action of their gradients through the primary Bjerknes force. In Refs. [4,7,25] it is shown that a modification in φ_b induces a change in the bubble position and enhances the emitted light, furthermore the presented results suggest the existence of an "optimum" phase value. However, the effect of P_{Ac}^{HF} on the positional instability can be negligible when the frequency of the harmonics is much higher than f_0 and the bubbles are not placed on the main pressure antinode, as we have shown in Ref. [22].

To the best of our knowledge, this is the first scientific work devoted to explain the role of both the frequency and φ_b of the harmonic pressure field P_{Ac}^{HF} in the context of bubble dynamics from a general point of view. The previous results reported in the scientific literature are limited to the exhibition of a particular bi-harmonic driving case.

In this work, we present an extensive parametric study consisting of both experimental results and numerical simulations in order to explain how different high frequency harmonic component constituting the bi-frequency acoustic driving signal affects the dynamics of sonoluminescent bubbles in H_2SO_4. In particular we will focus on the effect of the harmonic frequency used in P_{Ac}^{HF} (Nf_0) over the positional stability and the radial dynamics of bubbles trapped in a pressure field with spherical symmetry, ranging from the second to the fifteenth harmonic ($N = 2$—15). Additionally, we analyzed the dependence of the main physical bubble parameters on the relative phase between P_{Ac}^{LF} and P_{Ac}^{HF} for different values of N. These parameters were obtained through a numerical fit of the measured bubble radius temporal evolution (from now on $R(t)$) or by direct measurements of the bubble mean position (r_b) and its collapse time (t_c). Thus, we were able to analyze and correlate many important aspects of the phenomenon in a much broader way than previous works. Furthermore, the information provided by the experimental data was complemented (and extended) with the numerical simulations.

We also qualitatively discuss the role of the harmonic frequency in the generation of cavitation bubbles and their diffusive stability.

2. Experimental method

The experiments were made using the quartz spherical acoustic chamber (60 mm in outer diameter and approximately 1 mm in thickness) described in Ref. [19]. Details of the electronics and equipments employed can be found as well in Ref. [26,27] and references therein. The working fluid used was a highly degassed sulfuric acid aqueous solution 85% *w/w* (SA85) with relatively low concentrations (usually $c_\infty/c_0 \sim 15.10^{-3}$) of argon or xenon gas dissolved in the liquid. The resonance frequency of the apparatus for the lowest order radially symmetric oscillation mode with a pressure antinode near the geometrical center of the flask, was experimentally determined in approximately $f_0 = 29$ kHz. The driving system was composed of four equal piezoceramics transducers (PZT) attached to the outer wall of the resonator in diametrically opposed pairs. Two drivers (PZT_{LF}) were excited with the low-frequency signal ($V_{PZT}^{LF} = V_0 sin(2\pi f_0 t)$), while the remaining pair (PZT_{HF}) was used with the high-frequency signal ($V_{PZT}^{HF} = V_N sin((2\pi N f_0 t) + \alpha)$), which was a harmonic of f_0 (i.e. Nf_0). A disc shaped pill PZT was fixed to the resonator wall to be used as a microphone (MIC). In the experiments, the acoustic pressure field was set controlling the amplitude of V_{PZT}^{LF} and V_{PZT}^{HF}, f_0, Nf_0 and the relative phase between the signal components (α), which keep a linear relation with the signal picked by the MIC.

The bubbles were produced by acoustic cavitation near the center of the spherical resonator (were the main pressure antinode is located). The standard Mie scattering technique [28] was used to determine the temporal evolution of the bubble radius. The scattered light was captured using an *Oriel 77340* phototube connected to a *Hewlett–Packard HP 54615B* oscilloscope. The room temperature was controlled to be 297 K during the experiments. The experimental data traces were processed and fitted employing the numerical model of the bubble radial dynamics described in Ref. [29] which is based in the Rayleigh–Plesset–Keller equation (RPK). This model takes into account mass transfer effects at bubble wall (e.g. evaporation and condensation). Accordingly, in the simulations included in this study we have computed hundreds of acoustic cycles in order to ensure the bubbles diffusive stability. Furthermore, we have also considered the dissociation of the vapor diffused inside the bubble during the expansion phase, occurring in the bubble collapse. It is worth mentioning that in SA based systems the bubbles reach its equilibrium state (by rectified diffusion) in fewer cycles than in water based systems, mainly because of the low vapor pressure of the sulfuric acid aqueous solution. The latter also implies that in SA systems, there is a minor amount of water vapor to dissociate and/or produce chemical reactions than in water based systems [29]. All the assumptions in the model have been compared with a Navier–Stokes simulation (see Ref. [29]). The heat flux between the gas contents inside the bubble and the liquid were computed using the thermal boundary layer approxi-

mation as described in Toegel et al. [30] and Puente et al. [29]. The density, pressure and temperature are taken to be uniform within the bubble in the mentioned model. The validity of this assumption has been tested following the work of Lin et al. [31].

This model was also used to carry out some aspects of the numerical simulations presented in this work (e.g. hydrodynamic force fields and phase parameter spaces). The physical properties of the liquid used in the simulations are summarized in Table 1.

The position, stability and relative intensity of the studied SL bubbles, were evaluated through photographs captured by two cameras (*Nikkon D40x* and *Hitachi KP-F120*) set to take pictures from two orthogonal perspectives. Particularly, the observed bubble position was corrected taking into account the curvature of the spherical resonator wall and the changes in the refractive index of the propagation media. Furthermore, the tridimensional position was determined by means of a iterative triangulation algorithm.

The collapse time of the bubbles (t_c), defined as the time interval between the low frequency acoustic pressure zero crossing with negative slope and the SL flash emission, was measured with a timer *Stanford Research Systems SR620*. This apparatus was operated at its maximum sampling rate (≃1500 samples/s) with a precision of 100 ns (determined by the jitter in the MIC signal).

3. Results and discussion

This section describes and discuss a series of experiments and simulations designed to answer two main questions: Is there an optimum value of N and the relative phase φ_b in order to enhance the bubble stability and energy concentration? Is there any limit frequency in which the HF component of bi-harmonic driving P_{Ac}^{HF} cease to have a significant effect on the bubble dynamics? Unless otherwise specified, all the data presented in this study (both experimental measurements and numerical simulations) correspond to the case of single bubble sonoluminescence (SBSL). This part of the work is organized as follows: In Section 3.1, the central hypothesis is outlined by means of simulations of the radial dynamics of typical bubbles for different driving frequencies. Subsequently, we compare experimental traces of the $R(t)$ measured for bubbles subjected to different bi-harmonics pressure fields. Furthermore, the effect of φ_b on the bubble's stability is demonstrated through photographs. These findings motivated the realization of a series of numerical simulations in order to complement and also support the experimental observations. The numerical simulations, described in Sections 3.2 and 3.3, let us investigate many aspects of SBSL phenomenon under controlled and stable situations which are extremely difficult to achieve in the experiments. In Section 3.2, we discuss how the use of harmonics of different order N affects the positional stability of the sonoluminescent bubbles. On the other hand, the influence of φ_b in the $R(t)$ of a fixed bubble is explored in Section 3.3. Finally, in Section 3.4 we perform a multivariate analysis based on the covariance method to study the dependences among the experimental bubble parameters obtained from the numerical fits of the $R(t)$. In addition, we tracked the bubbles position on the acoustic chamber (r_b) in order to analyze their positional stability. The parametric analysis was complemented with extensive measurements of the collapse time of xenon bubbles carried out for different bi-harmonic drivings (N) and distinct relative phases set in the driving signal.

3.1. Qualitative experimental observations

One of the many aspects in which the driving frequency of the system plays a significant role is the diffusive stability of the bubbles. This topic has been broadly discussed in Ref. [8] for a case where the second harmonic was added to P_{Ac}^{LF} using water as the working fluid. In the experiments with SA85, we noticed that the presence of a high frequency component in the acoustic pressure field inhibits (or slows down) the bubble dissolution with respect to the case with single frequency driving. When the HF component P_{Ac}^{HF} was applied and P_{Ac}^{LF} was turned off, small bubbles could be found several hours after the remotion of the LF component, even in the cases with extremely low dissolved gas concentrations (e.g. $c_\infty/c_0 \leqslant 5\times10^{-3}$). Simulations of the R_0—$P_{Ac}|_b$ phase space for bubbles in SA85 driven only with P_{Ac}^{HF} set to different harmonics N (not shown) were ran in order to explain this phenomenon. The results indicate that an increment in the applied frequency produces a notorious reduction in the *bubble habitat*, being this in agreement with similar calculations performed by Koch et al. [38] for a case using water. As the frequency is increased, only bubbles with a small ambient radius can be trapped in the fluid as a consequence of the mass flux balance occurring in rectified diffusion.

Table 1
Physical properties of SA 85% *p/p* at 297 K [32–37].

Vapor pressure [Pa]	4.53
Density [kg/m^3]	1773.2
Speed of sound [m/s]	1513
Dynamic viscosity [Pa s]	0.022
Surface tension [N/m]	0.056
Specific heat [J kg^{-1} K^{-1}]	1829.2
Thermal conductivity [W m^{-1} K^{-1}]	0.3578
Refractive index	1.435

On the other hand, the addition of P_{Ac}^{HF} in the pressure field promoted the generation of multiple cavitation bubbles (as reported in Ref. [12]). Probably, this is due to the increased number of pressure antinodes distributed all over the resonator which can produce bubbles by means of the mechanisms described in Refs. [12,39,40], like the presence of colloidal particles acting as bubble "seeds".

The role of the driving frequency (f) in sonoluminescence can be studied by analyzing its effects on the bubble radial dynamics ($R(t)$). Generally speaking, when f is relatively low (compared to the linear resonance frequency (*Minnaert frequency*, f_M)) the fraction of the acoustic cycle in which the bubble remains in their expansion phase is relatively high, thus it reaches high values of R_{max}. Based on this argument one might say that when f is low there is a "good" coupling between P_{Ac} and the $R(t)$. Then, taking into account that the mechanical energy density is proportional to $(R_{max}/R_0)^3$, the use of low frequencies might seem to be an effective strategy to reach high energy focusing through violent bubble collapses [41]. In this situation, the pressure inside the bubble is very low for a long period of time and then there is an important flux of mass from the liquid towards the bubble core and its ambient radius (R_0) increases in each acoustic cycle, leading to a rapid bubble rupture because of the shape instabilities [14]. Consequently, the use of low driving frequencies do not represent a clear advantage [21]. Contrarily, if f is very high (e.g. of the order of f_M) there are factors like the fluid inertia and the reduced duration of the expansion phase, which limit the mechanical energy delivered to the bubble. In those cases the bubble oscillate with an almost linear dynamic and sonoluminescence can be only achieved for a very restricted region of the map of parameters R_0—$P_{Ac}|_b$ [42].

To illustrate the concepts discussed previously we plot in Fig. 1 (a) numerical results on the response of a typical bubble with $R_0 = 8$ μm driven using three different frequencies for a fixed pressure amplitude of $P_{Ac}|_b = 1.5$ bar. From the $R(t)$ curves is easy to see how the bubble dynamics rapidly become linear as f is increased. This is particularly noticeable in the lower values of R_{max} and the absence of bounces after the main bubble collapse.

From the preceding paragraph we might conclude that given R_0 and $P_{Ac}|_b$ there might exist an optimum frequency range in which the bubbles behave in a highly nonlinear fashion but still

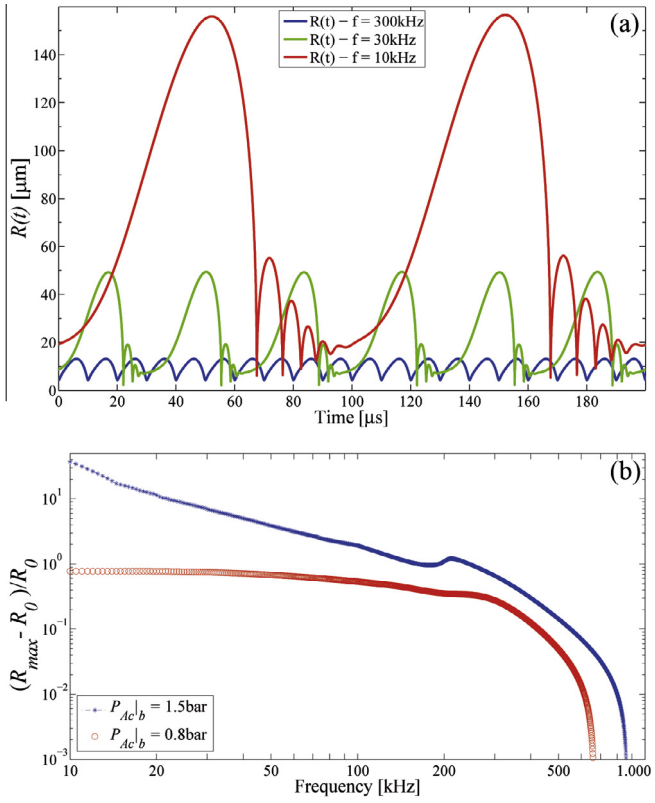

Fig. 1. Bubble dynamics for different driving frequencies in SA85. (a) Bubble radius temporal evolution for three distinct frequencies and a driving pressure amplitude of $P_{Ac}^{LF}|_b = 1.5$ bar. The maximum radius reached by the bubble decay notoriously as f is increased. (b) Frequency response curves (RPK model) for a bubble with a typical ambient radius of $R_0 = 8$ μm subjected to two different pressure amplitudes. The red (lower) curve correspond to a case were $P_{Ac}^{HF}|_b$ is below the Blake threshold, consequently the bubble is subjected to an almost linear oscillation, while the bubbles associated with the blue (upper) curve oscillate in a non linear fashion. The Minnaert frequency computed for a bubble under these conditions is $f_M = 320.8$ kHz. (For interpretation of the references to colour in this figure caption, the reader is referred to the web version of this article.)

remaining shape stable. The latter statement could not be rigorously accurate considering the existence of bubble nonlinear softening resonances as those observed in the case of water systems [2,42]. In order to study this phenomenon for the case of highly viscous fluids like SA85, we run simulations of the $R(t)$ of a bubble with $R_0 = 8$ μm and two distinct acoustic pressure amplitudes. In one case we choose $P_{Ac}|_b = 0.8$ bar to excite the bubble in an almost linear fashion (slightly below the Blake threshold) and in the other $P_{Ac}|_b = 1.5$ bar (far beyond the Blake threshold). It was numerically verified that all the simulated bubbles were shape stable. The expansion ratio $(R_{max}-R_0)/R_0$ obtained from these simulations are shown in Fig. 1(b) for the frequency range between 10 kHz and 1 MHz. In contrast to the observed in water based systems, the bubble do not exhibit sharp resonance peaks in none of the analyzed acoustic pressures. Except for a minor resonance peak near $f = 230$ kHz, the amplitude of the bubble oscillations decay monotonically with an increase in f. These phenomenon is closely related to the fact that SA85 is 25 times more viscous than water (hence the bubble behave more likely as a damped oscillator) and it has almost twice the density (thus it has more inertia).

In cases where bi-frequency driving is used, the effect of the harmonic component were examined by analyzing the shape of experimental traces of the $R(t)$. Fig. 2 presents data traces taken from similar bubbles ($\simeq R_0$) under comparable applied acoustic pressures $P_{Ac}^{LF}|_b$ (low-frequency) and $P_{Ac}^{HF}|_b$ (high-frequency) but using in each case a different N in the bi-harmonic driving. The bubble parameters were obtained from numerical fits performed with the RPK model [29]. Fig. 2 shows the typical signature of each harmonic in the $R(t)$ and how the influence of $P_{Ac}^{HF}|_b$ changes for different N. The main differences with the reference case ($N = 0$) can be summarized as follows: (1) The duration of the bubble expansion phase is visibly higher for lower harmonics. (2) Right after the first bounce, the $R(t)$ develops a series of fluctuations that increase their frequency and decrease their amplitude as N grows. (3) This undulatory pattern is also present during the bubble expansion and in its maximum radius R_{max}. The described pattern tends to disappear as the frequency of the harmonic moves away from f_0. Furthermore, there is a remarkable resemblance between the $R(t)$ measured with $N = 12$ and the one taken with a single frequency driving ($N = 0$). The latter become more evident in Fig. 3, which shows the root mean square difference of the $R(t)$'s displayed in Fig. 2 relative to the case with $N = 0$ (defined as $\int_0^\tau dt\sqrt{(R(t)|_N - R(t)|_0)^2}/(\tau P_{Ac}^{HF})$).

It is worth noting that the previous result imply an important experimental application for the use bi-harmonic driving. That is the possibility of using the effect of each frequency component of P_{Ac} independently, as we have already done in the experiments reported in Ref. [22] for an specific case where $N = 10, 11$ was used. In the latter, P_{Ac}^{LF} clearly dominated the bubble radial dynamics (and consequently determined the diffusive, positional and shape instabilities of the bubble), while P_{Ac}^{HF} mainly suppressed the spatial stability. Thus, the bubble can be fixed (and thus measured) through very high harmonic frequencies while its principal dynamical characteristics can be controlled adjusting P_{Ac}^{LF}.

Up to this point we have discussed the effect of P_{Ac}^{HF} analyzing only the role of the driving frequency. However, the relative phase (φ_b) between the two components of $P_{Ac}(\vec{r}, t)$ is another important factor that has to be considered. It should be noted the difference between φ_b and the relative phase between the components of the electronic driving signal (defined as α). While α is what we set externally in the customized signal generator system [26], the relative phase φ_b refers to the acoustic pressure field that actually affects the bubble. As detailed in Section 3.4, the original value of the phase α can be distorted by numerous factors like: the electronic setup (amplifiers, filters, PZT, etc.), the changes in the acoustic impedance of the parts that form the resonator and also by the bubble position [7] (among other things).

In the experiments we observed that a variation in α changes the bubble dynamics in a variety of aspects including the spatial stability, the equilibrium position and the light intensity emitted by the bubble. As been previously reported by Moraga et al. [7] and Krefting et al. [8], we also noticed that the changes took place smoothly and were reversible, which means that if α is varied from a certain value, the bubble recovers its original behavior once α is restored. In Fig. 4 we exhibit an example of these facts through a series of photographs showing the mentioned changes encountered as α was modified in a full cycle. It was common to find angular intervals where the bubbles were not luminescent or they dissolve (e.g. in Fig. 4 from 240° to 310°), specially for low order harmonics ($N = 2$–5).

The qualitative observations discussed in this sections motivated the realization of a parametric study, to analyze not only the bubble radial dynamics for different f, but also the effect of a variation in the relative phase φ_b and the role of each frequency component of the bi-harmonic driving on the hydrodynamic forces acting on the bubble.

3.2. Positional instability

In sonoluminescence systems with SA85 the action of the Bjerknes primary force imposes an upper limit in the low frequency

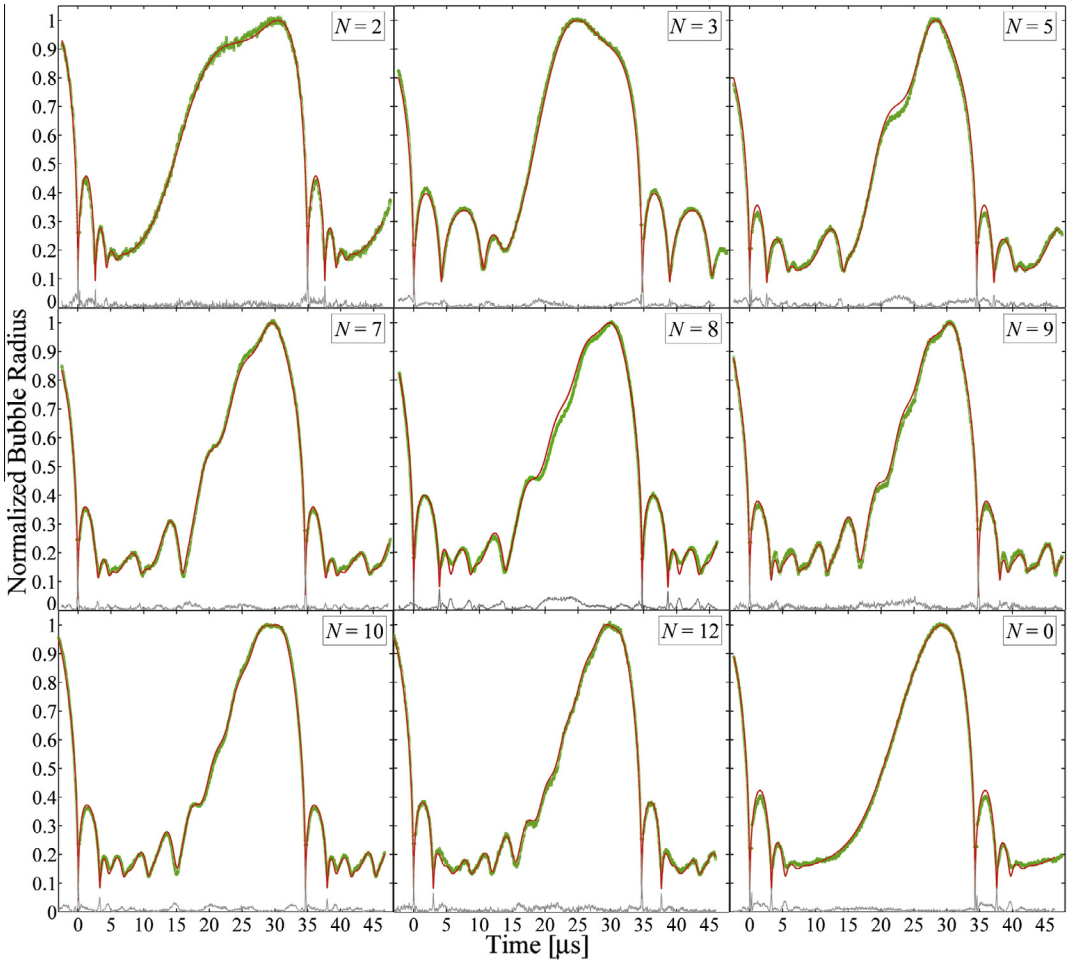

Fig. 2. Comparison of the normalized radius temporal evolution of argon sonoluminescent bubbles with similar R_0, driven with comparable acoustic pressures but using different high frequency harmonic components (Nf_0) in the bi-frequency driving signal. The characteristic parameters of each bubble were obtained from the experimental traces (circles) by means of a numerical fit (solid line).

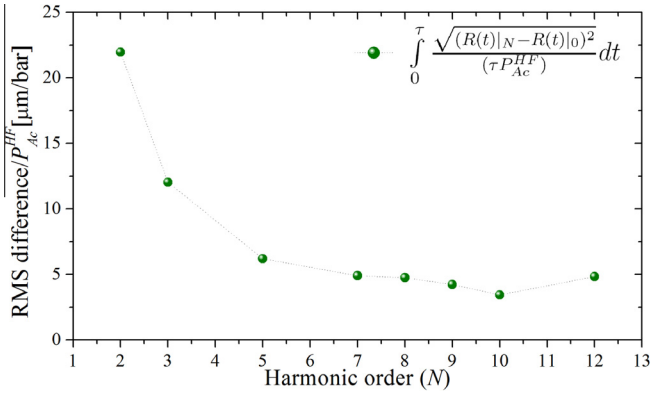

Fig. 3. Root mean square difference of the $R(t)$'s displayed in Fig. 2 with respect to the case with $N = 0$. This quantity was averaged in a period (τ_s) of the LF driving signal. Considering that each bubble have similar parameters ($R_0, P_{Ac}^{LF}|_b, P_{Ac}^{HF}|_b$) it is clear how the bubble radius temporal evolution become more likely to the one with single frequency driving as N grows. The computed relative error for the data points included in this figure was around 2%.

acoustic pressure that can be applied to the bubbles (i.e. $P_{Ac}^{LF}|_{F_b=0}$). This is actually an approximation since the threshold is determined by all the hydrodynamic forces acting on the bubble, as been evidenced in Refs. [19,22,24]. Considering a cavitation bubble initially located near the center of the resonator, the positional stability of the bubbles can be classified in three typical situations:

1. $P_{Ac}^{LF}|_0 > P_{Ac}^{LF}|_{F_b=0}$: If the low frequency acoustic pressure at the main antinode ($P_{Ac}^{LF}|_0$) is beyond the positional instability threshold, the bubble shifts its position away from the center in order to maintain the balance of the hydrodynamic forces affecting the bubble. This situation is clearly displayed in Fig. 15.
2. $P_{Ac}^{LF}|_0 \simeq P_{Ac}^{LF}|_{F_b=0}$: In this case, we set a LF pressure amplitude at $r = 0$ just on the positional stability threshold $P_{Ac}^{LF}|_{F_b=0}$. As this pressure produces a null value of the LF component of the hydrodynamic force acting on the bubble $\left(\langle \vec{F}_b^{LF} = 0 \rangle\right)$, the positional stability of the bubble must be uniquely determined by $\langle \vec{F}_b^{HF} \rangle$.
3. $P_{Ac}^{LF}|_0 + P_{Ac}^{HF}|_0 < P_{Ac}^{LF}|_{F_b=0}$: Here we adjust the pressure amplitudes of both frequency components (LF and HF) in order to guarantee the positional stability of the bubble $\left(\langle \vec{F}_b^{LF} \rangle + \langle \vec{F}_b^{HF} \rangle\right) < 0$, for all the harmonic frequencies used in the simulations. Hence, the bubbles settled over the main antinode remained in an equilibrium state.

Taking the latter into account, a systematic numerical study on the role of P_{Ac}^{HF} in the positional instability of the sonoluminescent

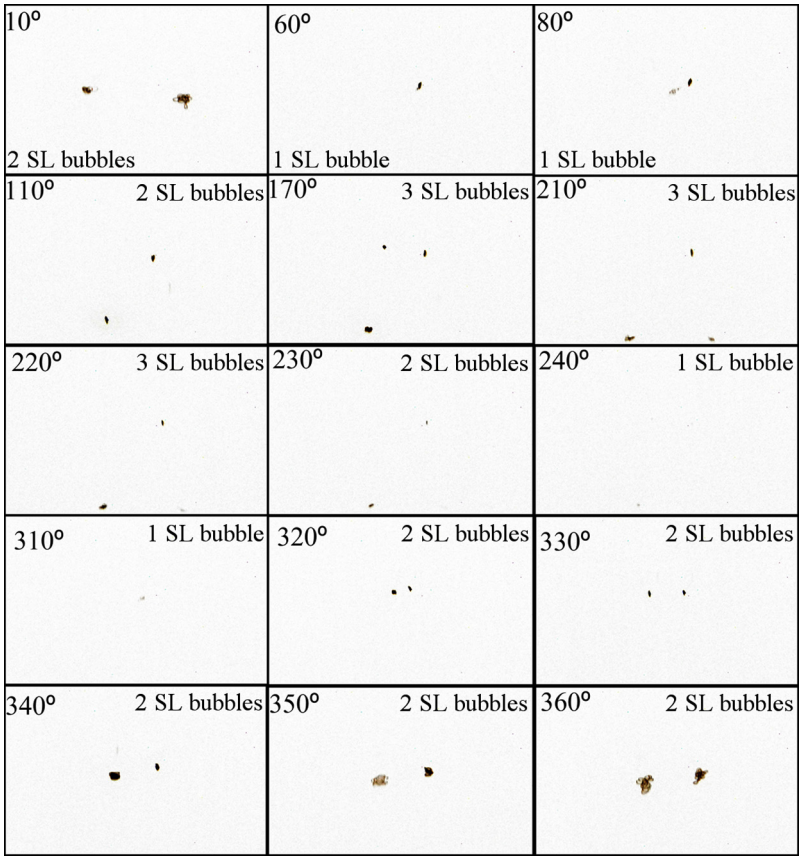

Fig. 4. Photographs of SL argon bubbles in a pressure field composed of a fundamental frequency f_0 and its third harmonic $3f_0$ for different α. The images are the monochrome negative of the original pictures taken with an exposure time of 333 ms. The bubbles recover they original behavior after the phase α was modified an entire period of the HF component (360°).

bubbles was made. This study was composed of a series of simulations of the forces acting on the bubbles in all three experimental scenarios described above, and using different harmonics applied to the driving signal.

3.2.1. Simulations for different harmonics in the driving signal

The numerical research was fulfilled by analyzing the main bubble parameters ($P_{Ac}^{LF}|_b, P_{Ac}^{HF}|_b, R_0, R_{max}/R_0, \dot{R}_{max}, T_{max}, t_c$). The positional instability was also discussed taking into account the three scenarios outlined in the previous section. In order to emulate the experimental conditions and procedures, the simulations were performed setting a fixed relative gas concentration dissolved in the fluid (c_∞/c_0) and assuming an acoustic pressure profile according to a particular "breathing" mode in the spherical resonant chamber. Thereby, only bubbles with dynamical parameters $R_0, P_{Ac}^{LF}|_b$ and $P_{Ac}^{HF}|_b$ over the selected isoconcentration curve were considered, and thus the diffusive stability of the computed bubbles was guaranteed.

All the simulations were carried out under the assumption of a complete translational stability of the bubbles, or a steady equilibrium paradigm. This means that the bubbles already passed its initial transient behavior and are settled on a fixed point of space [43,22]. It was also assumed a low gas concentration dissolved in the SA85 ($c_\infty/c_0 = 5 \times 10^{-3}$), which allows us to rule out the potential formation of orbits or significant displacements of the bubble [19]. Finally, the relative phase φ_b was fixed in 0° for all cases presented in the simulations of Figs. 7 and 8. In this way we can ensure that any observed change must be a consequence of the variation in the harmonic frequency only (and not φ_b).

The hydrodynamic forces affecting the bubble are: Bjerknes primary force, Added mass force, History force, Drag force and Buoyancy force. Because of the low values of c_∞/c_0 (and R_0) and the presence of high frequencies in the driving signal, the influence of the *history force* ($\vec{F}_{hist}$), the *viscous drag force* ($\vec{F}_{drag}$) and the *buoyancy force* ($\vec{F}_{grav}$) on the positional instability can be neglected [19,20]. Consequently, only the *primary Bjerknes force* ($\vec{F}_{Bj}$) and the *added mass force* ($\vec{F}_{am}$) were computed in the numerical procedures.

Sonoluminescent bubbles reach a positional stable state when the mean value of the net hydrodynamic force over a whole period of the LF acoustic cycle takes a null value (i.e. when $\langle \vec{F}_b \rangle = \langle \vec{F}_{Bj} \rangle + \langle \vec{F}_{am} \rangle = 0$), being:

$$\langle \vec{F}_{Bj} \rangle = -\frac{4\pi}{3\tau_s} \int_{\tau_s} (R(t))^3 \vec{\nabla} P_{Ac}(\vec{r}, t) dt \tag{1}$$

$$\langle \vec{F}_{am} \rangle = \frac{2\pi\rho_l}{3\tau_s} \int_{\tau_s} \frac{d\left[R(t)^3 (\vec{u}_l(t) - \vec{v}_b(t))\right]}{dt} dt \tag{2}$$

where τ_s present one period of the LF component of the driving signal, ρ_l is the liquid density, and $\vec{u}_l(t)$ is the instantaneous velocity of the liquid surrounding the bubble and $\vec{u}_b(t)$ is the velocity of displacement of the bubble.

First, we computed the acoustic pressure profile associated with different spherical modes corresponding to distinct harmonics N. Then, we traced a mesh of discrete equidistant points r_b along the resonator radius, where each position r_b was referred to a specific set of pressure amplitudes $P_{Ac}^{LF}|_b$ and $P_{Ac}^{HF}|_b$ as shown in

Fig. 5(a). Next, we simulated the bubble radius temporal evolution ($R(t)$), iterating the value of the ambient radius R_0 in some interval, for each discretized bubble position r_b. Only the values of r_b linked to pressures above the Blake threshold were computed.

The phase diagrams generated by parameters like R_0–$P_{Ac}|_b$ or R_0–φ_b are widely used to summarize the characteristics and stability of sonoluminescent bubbles [44,5,13,7,24,14,19]. In Fig. 5(b) we introduce a new kind of parameter map generated by the ambient radius R_0 and the bubble radial position (from now on r_b). It is worth noting that in a spherical resonator, the pressure amplitude profile associated with the first normal mode is monotonically decreasing, therefore we were able to replace the $P_{Ac}|_b$ axis by the radial coordinate r in the standard form of an R_0–$P_{Ac}|_b$ phase diagram. The main advantage of this type of map is to give a clear idea of the spatial locations accessible by diffusive stable bubbles with various sizes (R_0), which in addition favors the study of both, positional and shape instabilities. Furthermore, the R_0–r_b map can also include information about the maximum temperature reached by the bubbles or their collapse time. It is important to note that in this alternative diagrams, such as that presented in Fig. 5(b), each r_b value is related to a different $P_{Ac}^{HF}|_b$ while φ_b is fixed to given value (in Fig. 5(b) $\varphi_b = 0°$).

The first series of simulations was set up according to the cases previously labeled as (1) and (2). In those, we computed several R_0–r_b maps for a bi-frequency field composed by a fundamental frequency $f_0 = 29$ kHz and one of its harmonics defined between the second and the fifteenth ($N = 2$–15). For each discrete location r_b, we also calculated the net force ($\langle \vec{F}_b \rangle$) acting on a bubble with its ambient radius belonging to the curve with constant c_∞/c_0 (red line in Fig. 5(b)).

The integral that represents the mean value of the Bjerknes force (ec. (1)) over an acoustic period (τ_s) can be divided into two multiplicative terms. One has a spatial dependence given by $\vec{\nabla} P_{Ac}(\vec{r})$, while the other is purely a function of time, being defined as $f_{Bj} = \int_{\tau_s} (R(t))^3 P_{Ac}(t) dt$ [23]. Fig. 6 presents separate graphs of this two terms ($|\vec{\nabla} P_{Ac}(r)|$ and f_{Bj}) along with the $P_{Ac}(r)$ and the mean value of the force $\langle \vec{F}_{Bj} \rangle$ as a function of the radial distance to the center of the acoustic chamber r, for the cases corresponding to $N = 3$ and $N = 12$. The graphs in Fig. 6(a) and (b) correspond to case (1) in which the acoustic pressure amplitudes were set to $P_{Ac}^{LF}|_0 = 2$ bar and $P_{Ac}^{HF}|_0 = 1.5$ bar. The figures clearly expose that some regions (near $r = 0$) are not accessible to the bubble (for example the gray section of the curves in Fig. 6). Within these high pressure regions, two things can occur to the bubbles. On one side, the bubbles enlarge their R_0 in order to attain diffusive stability, leading them to their breakup under the action of shape instabilities (see Fig. 5(b)). On the other side, the positive sign of $\langle \vec{F}_{Bj} \rangle$ near the pressure antinode indicates that an eventual bubble would be repelled from that location. The graphs in Fig. 6(c) and (d) show a similar numerical simulation carried out for the second experimental scenario labeled as (2). Here we set the low frequency acoustic pressure amplitude just at the threshold where $\langle \vec{F}_b^{LF} \rangle$ changes sign while P_{Ac}^{HF} maintains the same value as in (1), that is $P_{Ac}^{LF}|_0 = 1.7$ bar and $P_{Ac}^{HF}|_0 = 1.7$ bar. In this situation (2) the positional stability of the bubbles located near the center of the resonator was mainly determined by $\langle \vec{F}_b^{HF} \rangle$, so there is more than one equilibrium position (r_{eq}) within the acoustic chamber. It is important to note that r_{eq} was defined in the locations where the total force acting over the bubble takes a null value ($\langle \vec{F}_b^{Total} \rangle = 0$), with negative slope to ensure an stable equilibrium (Fig. 6(d)).

Fig. 6 reveals that, regarding the positional stability, the "zone of influence" of P_{Ac}^{HF} is much lower than that of P_{Ac}^{LF}. That is because

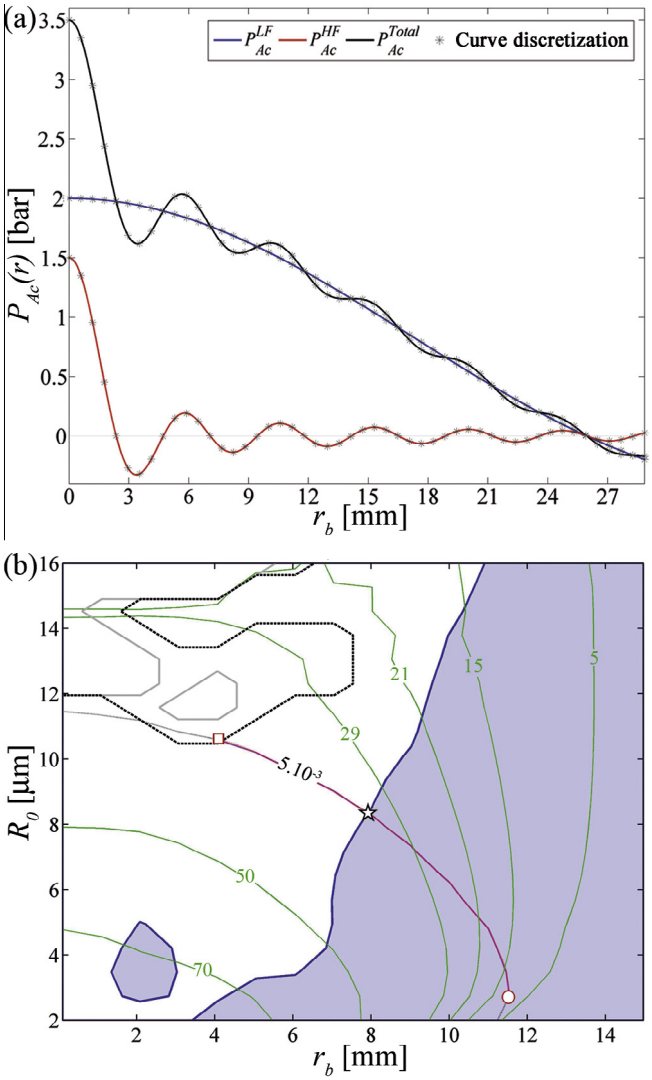

Fig. 5. Study of the stability of argon bubbles in SA85 under bi-harmonic driving ($\varphi_b = 0°$), considering radially symmetric modes of the acoustic resonator. (a) Pressure amplitude profile for a case where $f_0 = 29$ kHz and $N = 11$. (b) Phase space diagram R_0–r_b according to the acoustic pressure profile displayed in (a). The thin solid blue (black) line is the positional stability threshold ($\vec{F}_b = 0$). This line delimits the positionally stable region of the map (shaded in light blue (gray)) and the positionally unstable region (uncolored). The solid line in light gray is the Rayleigh–Taylor shape instability for the mode $n = 2$. The dashed black line corresponds to the parametric shape instability threshold. In the latter two curves, the stable region is always below the lines, or outside the closed curves. The green (gray) solid curves are the contours of constant T_{max} (in units of kK) and the thin dotted curves (black) are the contours of constant c_∞/c_0. The thick solid red (dark gray) line joining the circle and square markers indicates all the possible coordinate pairs in the R_0 where the bubbles are diffusively and shape stable for $c_\infty/c_0 = 5 \times 10^{-3}$. The star marker indicates the equilibrium position of the bubble. (For interpretation of the references to colour in this figure caption, the reader is referred to the web version of this article.)

both pressure components have different decay rates as r is increased. Considering a spherical acoustic chamber with radius a and a liquid where the sound velocity is c_s, the amplitude of P_{Ac}^{HF} decays as $\frac{a}{N\pi c_s r}$, while P_{Ac}^{LF} diminishes as $\frac{a}{\pi c_s r}$. An example of this can be found in Fig. 5(a), where the amplitude of $P_{Ac}^{HF} \ll P_{Ac}^{LF}$ for $r > 3$ mm. As a consequence, under the conditions stated in (1) the high frequency component of the acoustic field have a minor impact over the equilibrium position reached by the bubble (i.e. $\langle \vec{F}_b^{HF} \rangle \ll \langle \vec{F}_b^{LF} \rangle$), being more relevant for the spatial stability (reducing the formation of pseudo-orbits).

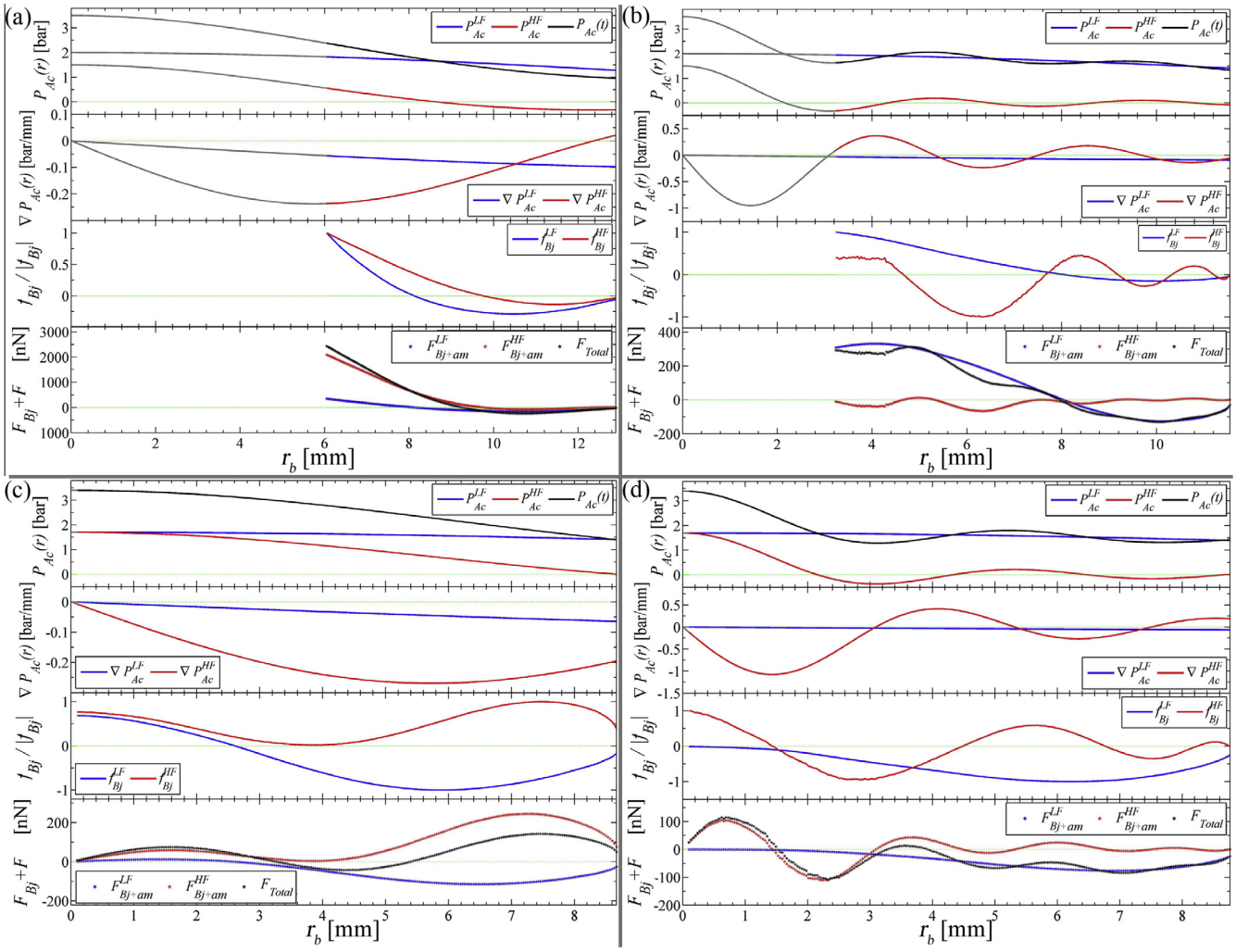

Fig. 6. Spatial distribution of the hydrodynamics forces (Bjerknes force and added mass force) for diffusively stable argon bubbles (with $c_\infty/c_0 = 5 \times 10^{-3}$) in a spherical resonator driven with $f_0 = 29$ kHz and several harmonics ($\varphi_b = 0°$). The gray lines represent regions where the bubbles can not exist due to the shape instability. In this figure, the data points plotted for f_{Bj}, F_{Bj} and F_{am} represent mean values, obtained integrating each force term in one period of the LF component of the bi-harmonic driving. (a) Here the pressure amplitudes in $r = 0$ mm were $P_{Ac}^{LF}|_0 = 2$ bar, $P_{Ac}^{HF}|_0 = 1.5$ bar, and the third harmonic of f_0 was used ($N = 3$). (b) $P_{Ac}^{LF}|_0 = 2$ bar and $P_{Ac}^{HF}|_0 = 1.5$ bar. In this case $N = 12$. (c) $P_{Ac}^{LF}|_0 = P_{Ac}^{HF}|_0 = 1.7$ bar and $N = 3$. (d) In this plot $P_{Ac}^{LF}|_0 = P_{Ac}^{HF}|_0 = 1.7$ bar and $N = 12$.

The module of the pressure gradient $|\vec{\nabla}P_{Ac}(r)|$ is a significant factor in the mean value of $\vec{F}_b$, since it acts as a weighting factor of the temporal parts of the computed forces f_{Bj} and f_{Am}. However, there were cases with $|\vec{\nabla}P_{Ac}(r)|_{N_1} \gg |\vec{\nabla}P_{Ac}(r)|_{N_2}$ (for $N_1 \gg N_2$), but where the net force $|\vec{F}_b|$ was greater for the lowest harmonic, being this a consequence of how P_{Ac}^{HF} modifies the $R(t)$ in a different way depending on the harmonic order used.

The characteristic physical parameters related to the equilibrium bubbles (located at distinct r_{eq}), studied in the scenarios (1) and (2), were compared in Fig. 7 for harmonics ranging from $N = 2$ to $N = 15$. The figure includes $P_{Ac}^{LF}|_b, P_{Ac}^{HF}|_b, R_0, \dot{R}_{max}$ and T_{max}. In the cases where multiple equilibrium positions were found, the closest r_{eq} to $r = 0$ was plotted. The simulated results exhibit a convergence of the analyzed parameters towards those found for the case with single frequency driving ($N = 0$), according the harmonic order was increased. This result was expected since, in the case labeled as (1), the bubbles reach equilibrium positions at radial distances r_{eq} outside the influence zone of P_{Ac}^{HF} for $N \geqslant 6$ (where $P_{Ac}^{HF} \ll P_{Ac}^{LF}$). For the second configuration (2) where $P_{Ac}^{LF}|_0 \simeq P_{Ac}^{LF}|_{F_b=0}$, the equilibrium position r_{eq} slowly approaches the resonator center ($r = 0$) while the rest of the parameters present the same converging behavior observed in (1) as N grows. Nevertheless, in case (2) the harmonic component effect on the bubble parameters can be noted even for high order harmonics like $N = 15$, being this in agreement with the variation found for $P_{Ac}^{HF}|_b$.

So far we have explored two scenarios ((1) and (2)) where the bubbles settle away from the main antinode, so the pressure amplitudes from both frequency components vary for each one of the bubbles analyzed. To conclude the present study on positional instability, we analyzed the remaining scenario designated by (3). In this situation, both components (LF and HF) of $\vec{F}_b$ are attractive to the antinode, hence the simulated bubbles are spatially, positionally and diffusively stable at the main antinode for all N. This implies that any observed change in the radial dynamics of the bubbles, must be a direct consequence of P_{Ac}^{HF} acting on the $R(t)$, independently of the spatial term $|\vec{\nabla}P_{Ac}(r)|$.

In the simulations performed for scenario (3), relatively low pressure amplitudes ($P_{Ac}^{LF}|_0 = 1.45$ bar and $P_{Ac}^{HF}|_0 = 0.25$ bar) were used in order to guarantee that the bubble would be trapped very close to the resonator center ($r_{eq} = 0.1$ mm) for all N. A set of the bubble parameters obtained from these numerical runs is shown

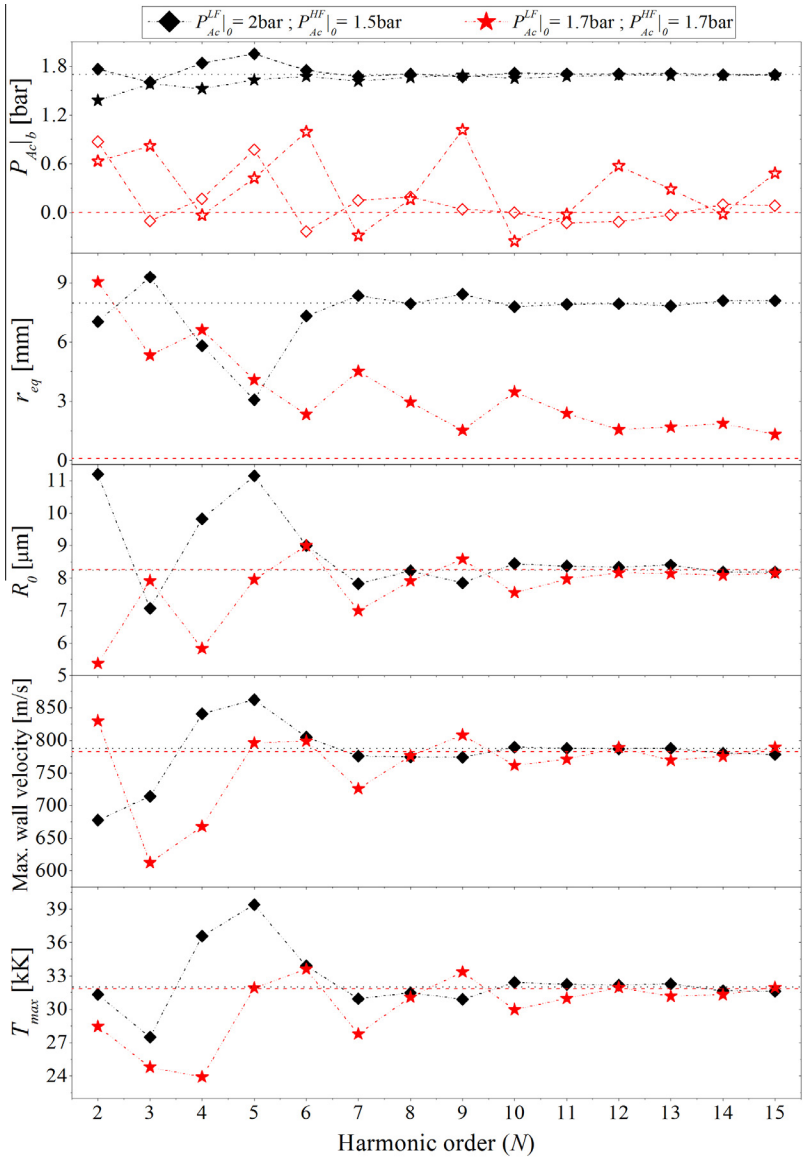

Fig. 7. Characteristic parameters related to the equilibrium bubbles simulated for a spherical bi-harmonic pressure field produced with a LF component (with f_0) besides distinct frequencies (Nf_0) set in the harmonic component. The fundamental frequency was set in $f_0 = 29$ kHz, while N was varied between the second and the fifteenth harmonic of f_0 ($N = 2$–15). The radial position of the bubbles r_{eq} was determined where $F_b = 0$ crossing with negative slope (see Fig. 6). The argon relative concentration were $c_\infty/c_0 = 5 \times 10^{-3}$. In the fist subplot, the filled markers correspond to the values of $P_{Ac}^{LF}|_b$ and the hollow markers represent $P_{Ac}^{HF}|_b$. The dotted horizontal lines indicates the value of each parameter obtained for the case with single frequency driving ($N = 0$).

in Fig. 8. As found in scenarios (1) and (2), the results demonstrate that when the HF component of the bi-harmonic driving has harmonic frequencies far above f_0, it does not significantly modify the bubble dynamics. Furthermore, as the harmonic frequency is increased, the average value of P_{Ac}^{HF} tends to zero when is integrated within one period of P_{Ac}^{LF}. These results have a great practical value implication: the possibility to control the spatial instability (through P_{Ac}^{HF}) and the bubble characteristics ($R(t)$) independently (as we did in Ref. [22] for a case with $N = 11$).

3.3. Effect of varying the relative phase φ_b

As we have shown through the photographs presented in Fig. 3, a change in the relative phase of the driving signal (α) affects both, the spatial and positional instabilities and the intensity of the emitted light. In many cases, the bubble moves along the azimuthal angle describing an arc segment. An example of this can be seen in Fig. 9, which displays the coordinates of a SL bubble whose position was tracked during a continuous sweep of α. This kind of behavior indicates that the HF component can excite non axisymmetric modes of the spherical resonator. In an finite thickness wall acoustic chamber, the resonant frequencies corresponding to radially symmetric modes (breathing modes) do not exactly match the harmonic frequencies of f_0 [45]. Thus, in order to explain the bubble positional excursions we must analyze the solution of the HF component of the pressure field for a case without azimuthal symmetry [27,46]:

$$P_{Ac}^{HF}(r,\theta,\phi,t,\varphi) = P_{Ac}^{HF}|_0 j_l(k_{ln} r)\, e^{i m \theta}\, P_l^m(cos(\phi))\, e^{i(N\omega t+\varphi)} \quad (3)$$

It is worth noting that in the non-radially symmetric modes (where $m \neq 0$), the gradient $|\vec{\nabla} P_{Ac}(r,\theta,\phi)|$ has radial and also angular components, which explains the bubble path displayed in Fig. 9.

As has been mentioned in Section 3.2.1, the Bjerkes force depends on both spatial and temporal terms (i.e. the pressure

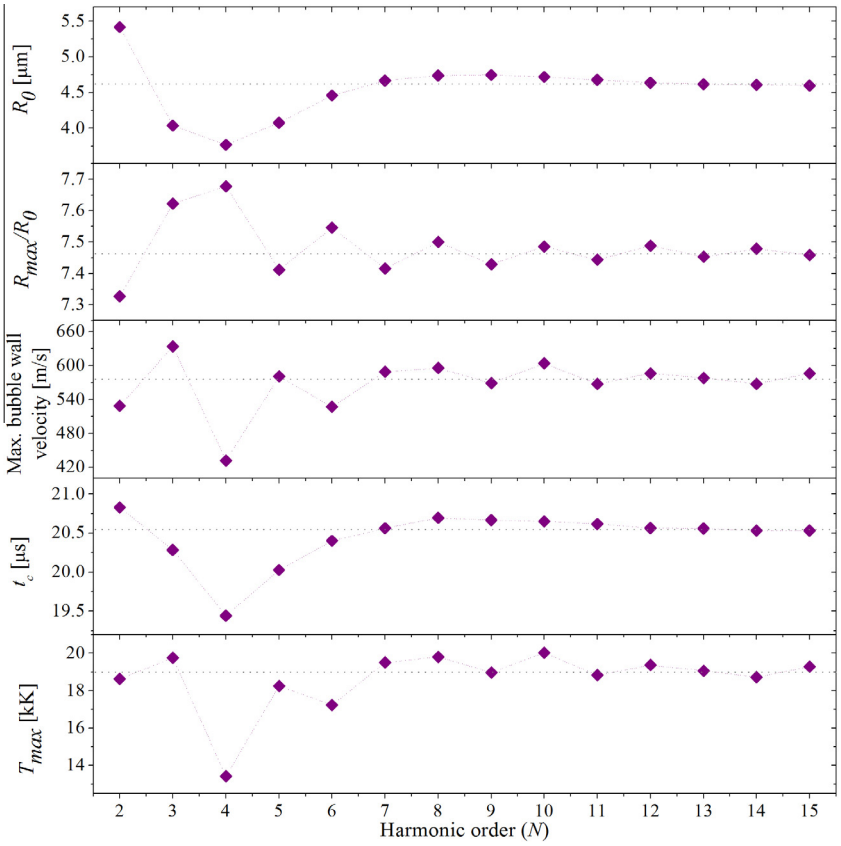

Fig. 8. Simulated characteristic parameters of equilibrium bubbles driven with different harmonics and located over the main pressure antinode ($r_{eq} = 0.1$ mm). Similarly to the calculations in Fig. 7, $c_\infty/c_0 = 5 \times 10^{-3}$ and $f_0 = 29$ kHz. The harmonic frequency component (given by Nf_0) was varied between $N = 2$ and $N = 15$. In this case the pressure amplitudes were adjusted to relatively low values to guarantee the positional stability of the bubble independently of which N is being used, hence $P_{Ac}^{LF}|_0 = 1.45$ bar and $P_{Ac}^{HF}|_0 = 0.25$ bar. The bubble parameters become independent of the harmonic order at high N values. This is mainly because the fluctuations induced on the bubble radial dynamics ($R(t)$) by the driving harmonic component turns to be negligible as they approaches to a linear regime.

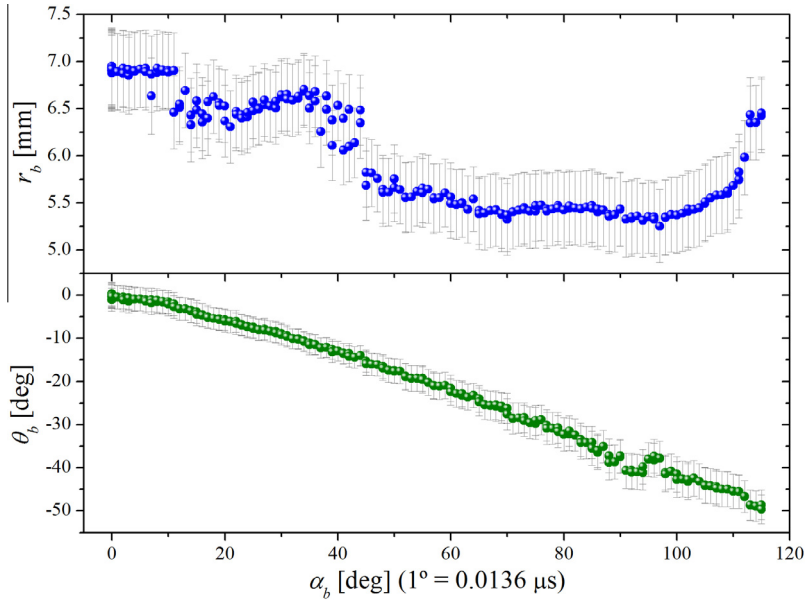

Fig. 9. Experimental position of a single SL argon bubble as a function of the relative phase between the two components of the driving signal (α) generated with $f_0 = 29.15$ kHz and $N = 7$. Here r_b is the radial distance to the resonator center and θ_b the azimuthal angle. The value of α is relative to the high frequency component V_{PZT}^{HF}. There is a smooth displacement in the bubble position. The angular shift shows that in many cases V_{PZT}^{HF} excites non spherical acoustic modes. The change in both radial and angular coordinates can also imply an alteration in the $R(t)$ and consequently in the hydrodynamic forces acting over the bubble.

gradients and $f_{Bj} = \int_{\tau_s} (R(t))^3 P_{Ac}(t)dt$). The phase φ_b only appears in the temporal part of P_{Ac}^{HF}, then a change in φ_b produces a direct variation in $P_{Ac}^{HF}(t)$. However, it also induces a change in the $R(t)$ affecting not only f_{Bj}^{HF} but f_{Bj}^{LF}, in addition. Thus φ_b is a relevant parameter, affecting all the forces involved in the positional instability. Since the impact of P_{Ac}^{HF} on the $R(t)$ of the bubbles becomes less significant as Nf_0 increases, we might expect that the response of the system to changes in φ_b decays in the same proportion for $N \gg 1$.

A more detailed analysis of the relation between the positional instability and φ_b can be done by means of R_0–φ_b phase diagrams [5] as that presented in Fig. 10, computed for a bubble settled over the main antinode of an acoustic field generated with $f_0 = 29$ kHz and $N = 5$. The relative phase φ_b was defined as positive when the high frequency was advanced with respect to the low frequency. Fig. 10 was obtained using the same set of parameters as in Fig. 8, which corresponds to the limit case (3) where the bubble remains stabilized near $r = 0$ ($\langle \vec{F}_b \rangle \sim 0$). The results of the simulation shown in Fig. 10 revealed the changes occurring in R_0 and T_{max} when φ_b is modified. Moreover, it shows the existence of regions of the R_0–φ_b parameter space where the bubbles can not exist in a stable fashion, being this in agreement with our observations in the experiments (e.g. Figs. 4 and 9). According to R_0–φ_b maps, where higher N cases were computed, the unstable regions in the maps were reduced to a series of narrow bands as N was increased.

3.3.1. Simulations varying φ_b for different values of N

The measurements discussed in the previous sections, were complemented with simulations designed to numerically explore the role of φ_b on the bubble radial dynamics for different harmonics constituting the high-frequency component of the bi-harmonic acoustic field. Here we used once again the scenario (3).

Following the same procedure applied in Section 3.2.1, we simulated bubbles with R_0 belonging to the contour of constant relative gas concentration $c_\infty/c_0 = 5 \times 10^{-3}$, sweeping the relative phase between 0° and 360° in regular steps (see Fig. 10). This numerical scheme was repeated for harmonics ranging from $N = 2$ to $N = 15$. We evaluated not only the characteristic bubble parameters (R_0, R_{max}, t_c and T_{max}) but also the mean value of the force produced on the bubble by each frequency component (i.e. $\vec{F}_b^{LF}$ and $\vec{F}_b^{HF}$). The outcome of these simulations are displayed in Fig. 11. This plot includes the maximum value, the minimum value and the standard deviation (STD) found for each parameter, obtained in an entire high frequency acoustic cycle (τ/N). This way of displaying the data emphasizes the fact that φ_b becomes irrelevant as N is increased. On the other hand, the results also infer that controlling φ_b may be a useful experimental technique to confine the bubble (setting $|\vec{F}_b|$ to be attractive) when low order harmonics are used (e.g. $N = 2, 3$). Furthermore, Figs. 10 and 11

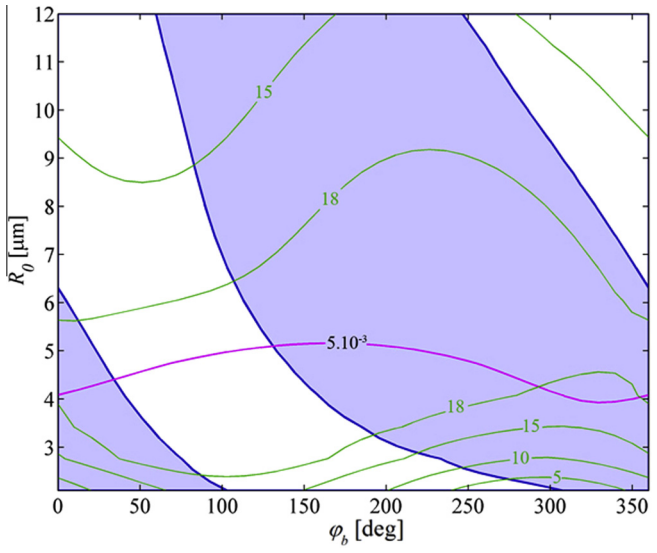

Fig. 10. Phase diagram R_0–φ_b for a spherical acoustic pressure field generated by f_0 and $N = 5$. The coding of the map is the same used in Fig. 5(b). The pressure amplitudes set in this simulation are taken from the case presented in Fig. 8 ($r_b = 0.1$ mm, $P_{Ac}^{LF}|_0 = 1.45$ bar and $P_{Ac}^{HF}|_0 = 0.25$ bar).

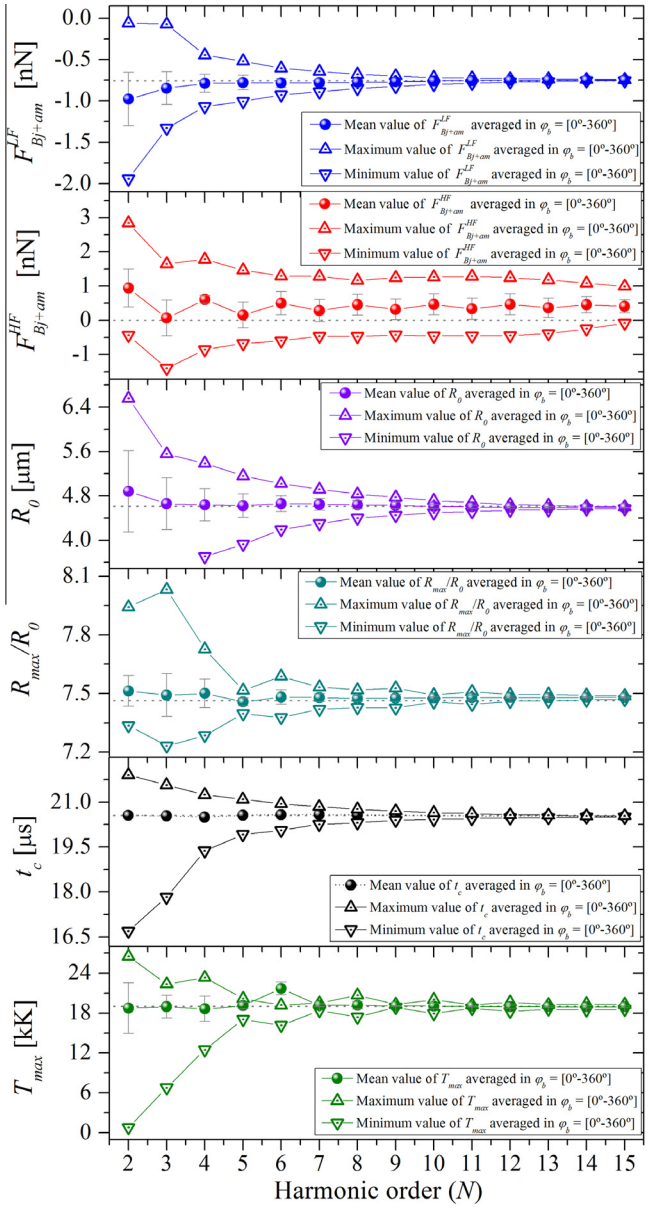

Fig. 11. Numerical simulations of the typical parameters of an argon bubble driven with a bi-frequency driving, composed by a LF component (of frequency f_0) and a HF component corresponding to a harmonic of f_0 (Nf_0) ranging from $N = 2$ to $N = 15$. The bubble was located near the resonator center at $r_{eq} = 0.1$ mm. Here $c_\infty/c_0 = 5 \times 10^{-3}$ and the fundamental frequency was $f_0 = 29$ kHz. The relative phase φ_b was iterated between 0° and 360° (that is a whole cycle of P_{Ac}^{HF}). The pressure amplitudes were $P_{Ac}^{LF}|_0 = 1.45$ bar and $P_{Ac}^{HF}|_0 = 0.25$ bar. The dotted horizontal lines represent the value of each parameter obtained for the case with single frequency driving ($N = 0$). The error bars are the standard deviation of the data linked to each harmonic.

show that a change in φ_b could produce an increase in the maximum temperature reached by the bubble during the collapse.

3.4. Parametric analysis of experimental bubbles

In this section we present experimental data mainly composed by series of measurements of the $R(t)$ of non-moving (spatially stabilized) argon SL bubbles subjected to various bi-frequency drivings, generated with different harmonics Nf_0 and several driving phases α, besides fundamental frequency (f_0). Additionally, we carried out extensive measurements of the collapse time t_c of moving (pseudo-orbits) SL bubbles in the case of Xe-SA85 system.

In order to generate experimental observations suitable to perform a straightforward comparison with the simulations shown in Figs. 6–8, we would be able to know precisely and control the acoustic field at the bubble position r_b and the resonator center (i.e. $P^{LF}_{Ac}|_{0,b}, P^{HF}_{Ac}|_{0,b}$ and φ_b). However, it is difficult to the bubble acoustic environment without the measurement and subsequent fitting of the bubble radius temporal evolution $R(t)$, as each bi-harmonic driving can excite different radially and/or non-radially symmetric HF modes (see Fig. 9). On the other hand, to measure the $R(t)$ by means of the Mie scattering technique, the bubble must be fixed (without pseudo-orbital movement). Moreover, in SA85 the spatial stabilization of the SL bubbles requires a fine tuning of $V^{LF}_{PZT}, V^{HF}_{PZT}$ and φ_b [19]. Thus, this procedure prevent us from developing a precise control on the bubble final position and the values of the bubble physical parameters. As a consequence, we were not able to experimentally reproduce the situations analyzed numerically in Figs. 8 and 11.

As an alternative approach, we opted to measure the $R(t)$ of a large number of spatially stabilized SL bubbles and then gather information regarding the system behavior by means of statistical tools (like STD or multivariate correlation analysis). Consequently, we measured the bubble radius temporal evolution $R(t)$ of spatially fixed argon bubbles driven with different harmonics, and then characterized them obtaining a series of parameters through numerical fits. Specifically, these bubble parameters can be summarized as follows: R_0, the expansion ratio $R_{max}/R_0, P^{LF}_{Ac}|_b, P^{HF}_{Ac}|_b$, the relative gas concentration c_∞/c_0, the collapse time t_c, the bubble wall velocity $\dot{R}(t)$, the mechanical energy density

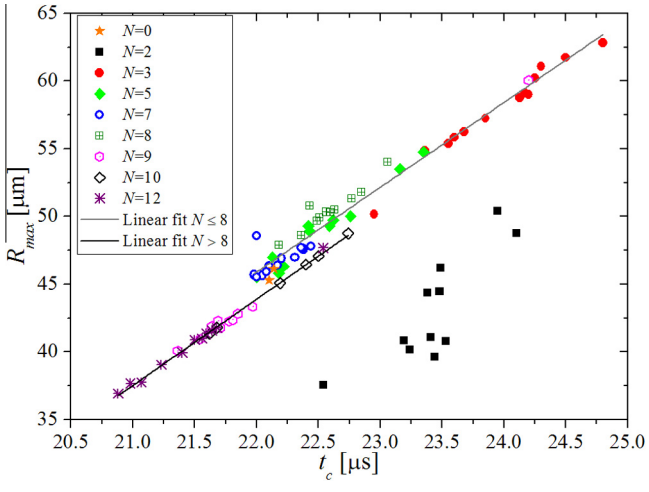

Fig. 12. Maximum bubble radius vs. collapse time for experimental argon bubbles driven with distinct N and φ_b. The gray and black lines represent a linear fit of the data taken with $N \leqslant 8$ (without $N = 2$) and $N > 8$ respectively. In both cases the fitted slope was (6.3 ± 0.1) m/s. Remarkably, the data for $N = 2$ have a different trend from the rest od the data. The relative error obtained for R_{max} was $\Delta R_{max} = 2\%$, while for the collapse time $\Delta t_c = 0.05$ μs.

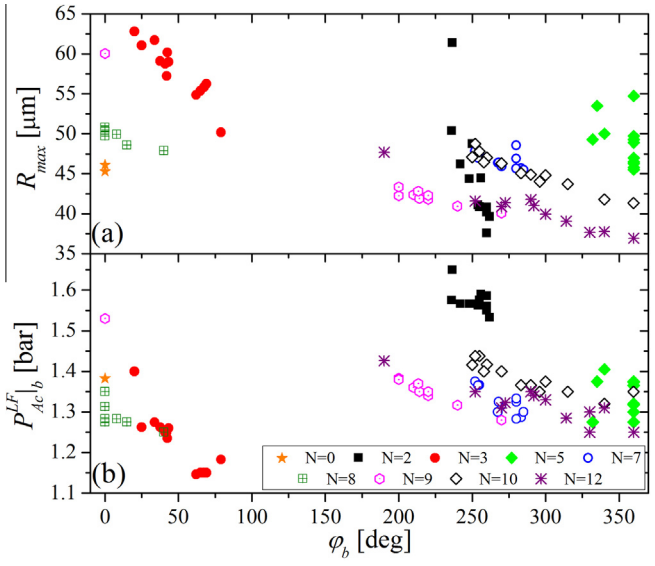

Fig. 13. Maximum bubble radius and low frequency component of the acoustic pressure field as a function of the relative phase φ_b for experimental argon bubbles driven using a distinct harmonic order N. (a) R_{max} vs. φ_b. (b) $P^{LF}_{Ac}|_b$ vs. φ_b. Both plots show the high degree of correlation between the parameters and how they decay as φ_b is increased. In this figure, the relative error associated to each parameter was $\Delta R_{max} = 2\%, \Delta P^{LF}_{Ac}|_b = 3\%$ and $\Delta\varphi_b = 2\%$.

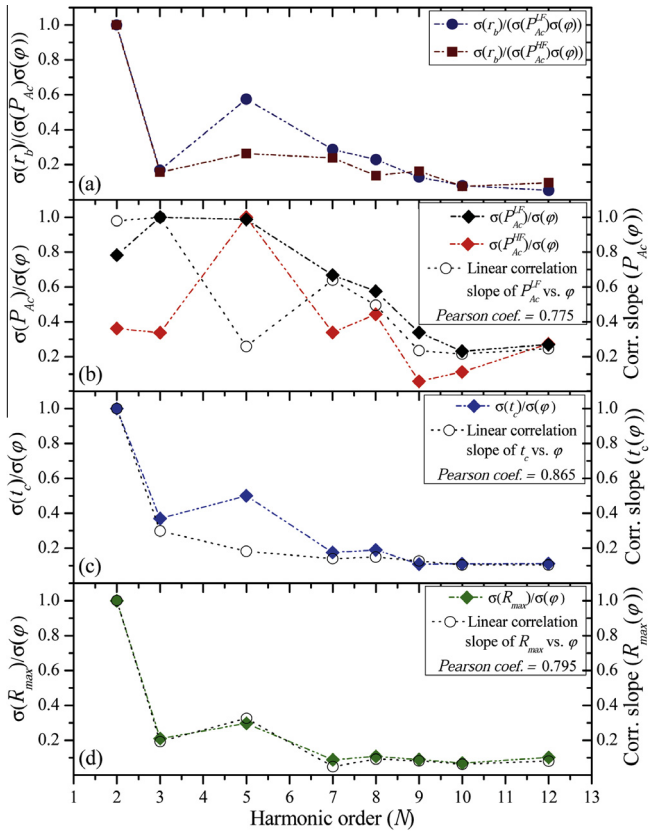

Fig. 14. Normalized ratios between the standard deviation of $P^{LF}_{Ac}, P^{HF}_{Ac}, t_c, R_{max}$ and r_b, relative to the deviation found in φ_b for the measured SL bubbles driven with distinct N. These statistical quantities point out how susceptible is a certain parameter to changes in φ_b. Moreover, the high values found for the mean value of the Pearson coefficient (close to the unity) indicate that there is a linear correlation between the data displayed in the three upper graphs and the relative phase. The decay observed in the normalized slope of the correlated quantities for higher harmonics demonstrate that the influence of φ_b also decreases.

$P_{Ac}^{LF}|_b\,(R_{max}/R_0)^3$, the maximum temperature of the gas/plasma T_{max}, f_0, the harmonic frequency Nf_0 and φ_b. In addition, we tracked the bubble position in the acoustic chamber in pursuance of analyzing their positional stability. We measured more than 130 SL bubbles driven with harmonics between $N = 2$ and $N = 12$ (approximately 13 $R(t)$ per N). For each N, the external relative phase α was varied in steps of 30°.

A multivariate analysis based on the covariance method [47] was implemented to study the relation among the parameters characterizing the SL bubbles. Particularly, we computed the Pearson's correlation matrix (obtained from the sample covariance matrix following Eq. (3.83) of Ref. [47]) and the spectral decomposition of the sample covariance matrix in order to quantify the degree of correlation and the slope corresponding to the linear dependence for each parameter pair.

A strong correlation was found between the maximum radius reached by the bubbles R_{max} and the collapse time t_c. As shown in Fig. 12, this quantities were related by a linear dependence with the same slope for all the harmonics (N). Remarkably, all the bubbles studied in this research exposed the same linear behavior as that observed in the Rayleigh collapse of an empty cavity [42], considering the broad variety of driving conditions in which the current bubbles were measured. Regarding to the Rayleigh case, the calculated slope R_{max}/t_c for a pure inertial (undriven) collapse in SA85 and a static pressure of $P_0 = 925$ mbar is 7.915 m/s, while the linear fit applied to the data in Fig. 12 produced a slope of (6.3 ± 0.1) m/s. In relation to the energy concentration reached by the bubbles in the collapse, we found a correlation between the maximum collapse velocity $\dot{R}_{max}$, the maximum temperature T_{max} and the mechanical energy density $P_{Ac}^{LF}(R_{max}/R_0)^3$, being these parameters proportional to each other. From the experiments, we also detected that those three variables have a non linear relation with the relative gas concentration c_∞/c_0, in agreement with the reported in Ref. [21] for bubbles with different P_0. The results show that SL bubbles achieve violent and hotter collapses as the amount of gas inside the bubble is decreased, in agreement with the results in Ref. [19].

The correlation analysis also revealed that the relative phase φ_b is closely related to important parameters like $R_{max}, T_{max}, R_{max}/R_0, t_c$ and the acoustic pressure P_{Ac}^{LF}. It was remarkable to find that these parameters always decrease as φ_b increases, as shown if Fig. 13 for R_{max} and P_{Ac}^{LF}. Since we were not able to explore a whole cycle fo the HF driving component in any of the studied cases, we did not observe a periodic dependence of the aforecited parameters on φ_b as it was reported for positionally stable bubbles in Ar–Water systems in Ref. [8]. The experimental results show a clustering in the values found for the relative phase φ_b. These values were confined within intervals with widths of 40° to 100° depending on the harmonic order N (see Fig. 13). The latter agrees with the simulation depicted in Fig. 10 which shows that the bubbles can not exist in a stable fashion for all the values of φ_b (uncolored regions) and also the trials presented in Fig. 2. The role of the positional instability in the definition of the bubble equilibrium parameter values must be taken into account to give a proper explanation of this phenomenon, considering the case of acoustic pressure profiles with radial and also angular dependencies.

Regarding to the spatial distribution of the bubbles in the acoustic chamber, they were grouped in clusters, whose extent changed according to which harmonic frequency was used. This fact reinforces the idea that the acoustic field is not axisymmetric.

As a way to estimate how sensitive was each parameter to changes in φ_b, we computed the ratio between the STD of each variable and the STD found for φ_b. This fluctuation analysis can be useful in cases like this, where some of the variables are related

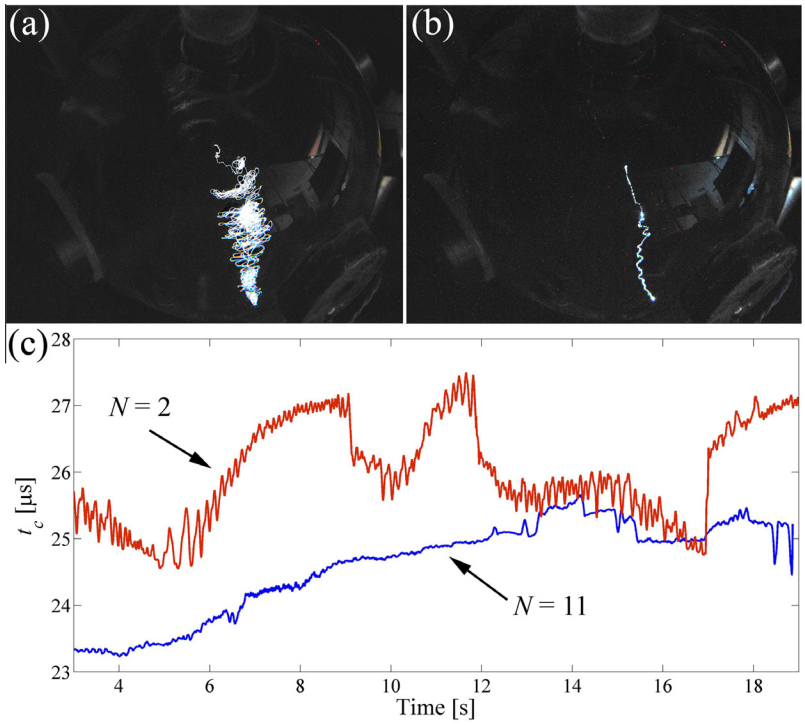

Fig. 15. Position and t_c of SL bubbles in a Xe-SA85 system for a ramp in the low frequency driving amplitude $V_{PZT}^{LF}(P_{Ac}^{LF}|_0)$ and $V_{PZT}^{HF} \simeq 80\ V_{rms}$. Here we used a fundamental driving frequency of $f_0 = 29$ kHz. Both photographs were taken with an Iso level of 3200 and 30 s of exposure time. (a) Typical behavior of a moving (spatially unstable; describing pseudo-orbits) SL bubble during the pressure ramp (single-frequency driving and $c_\infty/c_0 > 10^{-3}$ [27]). (b) Typical displacement of a spatially fixed (non-moving) SL bubble during the pressure ramp (single-frequency driving and $c_\infty/c_0 < 10^{-3}$ [27]). (c) Evolution of the collapse time for two bubbles driven with $N = 2$ and $N = 11$. The initial value of $P_{Ac}^{LF}|_0$ in the ramps was the minimum pressure in which the bubble get positionally unstable (close to the Bjerknes frontier). The relative gas concentration was $c_\infty/c_0 \sim 12.10^{-3}$.

in a highly non linear fashion and the correlation analysis fails. Fig. 14 presents values for the STD ratio of $P_{Ac}^{LF}, P_{Ac}^{HF}, t_c, R_{max}$ and r_b relative to the deviation in φ_b for SL bubbles driven with a different high-frequency component (Nf_0) applied in the bi-harmonic driving. The parameters that presented a little spread compared to that observed in φ_b, must have a negligible dependence on the relative phase. In particular, the positional stability of the bubbles was analyzed in Fig. 14(a). In this figure, the spread in the bubble position r_b was compared with a product of the STD of P_{Ac}^{LF} and STD of φ_b, being those the most relevant parameters regarding to the modification of the bubbles equilibrium position (as shown in Figs. 9 and 15). As shown in Fig. 14(a), the third harmonic pulls the SL bubble toward the center of the resonator whereas the opposite behavior (repulsive) was observed for $N = 2$ and $N = 5$.

The dependence among the measured bubble parameters was also analyzed by means of the Pearson's product–moment correlation coefficient. This coefficient together with the correlation slope, computed from the largest eigenvalue of the sample covariance matrix, quantify the degree of linear dependence between the parameters taken in pairs. It was found, that many parameter pairs have Pearson's coefficient with values close to the unity, indicating a strong linear correlation between the data points. Some examples of those measurements are shown in the subplots (b)–(d) of Fig. 14. In this figure, the decay observed in the STD ratio and the normalized slope of the correlated quantities for higher harmonics, is in agreement with the numerical simulations, showing that the relative phase becomes irrelevant to the bubble radial dynamics as the harmonic frequency augments. In particular, it is worth noting that despite of the regular spread and the lack of correlation observed between $P_{Ac}^{HF}|_b$ and φ_b for all N, the LF acoustic pressure $P_{Ac}^{LF}|_b$ did not vary considerably for higher harmonics, then the HF component has little influence on the Bjerknes frontier in those cases.

The linear correlation found between t_c and many relevant bubble parameters makes it an ideal control variable to characterize the system, since it can be directly measured for moving and non-moving SL bubbles without the requirement of fitting the bubble radius temporal evolution $R(t)$. Therefore, we carried out measurements of t_c employing a different and independent experimental method. The main advantage of this alternative system rely on its increased statistical weight and the fact that t_c is measured directly from the bubble flashes and the MIC signal using a timer. In this experiment we used xenon gas dissolved in the liquid ($c_\infty/c_0 \sim 12.10^{-3}$) in order to enhance the emitted light intensity allowing us to capture flashes from a bubble in its dimmer state. The measurements were taken following the same procedure applied in Ref. [19], that is, acquiring an important number of samples of t_c (over 20,000 values) during a pressure ramp applied to the resonator containing a single SL bubble. Here we repeated this method seven times for each bi-harmonic driving constituted by high-frequency components (Nf_0) ranging from $N = 2$ and $N = 12$, varying the external phase φ_b in 60° for one ramp to another. It is important to note that not only the pressure amplitude is modified during the ramps but also the relative phase of the acoustic field. Thus, this measuring protocol allows us to cover a wide range of possible values of φ_b that were attainable in the experiment. The initial value of $P_{Ac}^{LF}|_0$ in the ramps was defined as the minimum pressure in which the bubble got positionally unstable (close to the Bjerknes frontier). As the pressure was increased, the bubble average position shifted outward the resonator center in order to conserve the equilibrium of forces [24,22]. Fig. 15 shows the typical behavior of a moving (spatially unstable) SL bubble (Fig. 15) and the displacement of a non-moving SL bubble (Fig. 15(b)) during the pressure ramps. These two experimental situations, obtained in the Xe-SA85 system using two different dissolved gas concentrations and a single-frequency driving [19], were reproduced here using two different bi-harmonic drivings and the same $c_\infty/c_0 \sim 12.10^{-3}$. The ripples in t_c displayed in Fig. 15(c) were directly related to the spatial stability of the bubbles, which depends on both φ_b and $P_{Ac}^{HF}|_0$. In this example, the evolution of the collapse time for a bubble driven with $N = 2$ evidences an undulatory pattern whose frequency and amplitude are consistent with the orbits described by the SL bubble, contrarily to the observed for the case with $N = 11$ where the bubble was spatially stabilized (without pseudo-orbits). On the other hand, the discontinuities (jumps) exhibited in the curves of Fig. 15(c) are related with the sudden displacements of the SL bubble during the pressure ramp [19].

Fig. 16(a) presents a summary of the measurements of the averaged t_c values made employing distinct harmonics in the Xe-SA85 system. In this figure, the spread in t_c found for each N, is given by the standard deviation together with the difference between its maximum and minimum. It is worth noting that both quantities are determined not only by the sweep in φ_b but also the ramp in $P_{Ac}^{LF}|_0$. Then, considering that the range pressure amplitudes applied in each case (i.e. using different harmonics in the HF component of the bi-frequency driving signal) were very similar, and the value of t_c is dominated by the LF component of the acoustic field, is expectable to find equivalent spreads in t_c for all harmonic orders N. These results were compared with the ones obtained from the fitted $R(t)$ corresponding to SL bubbles in the Ar-SA85 system (Fig. 16(b)). The experimental data acquired by both methods have

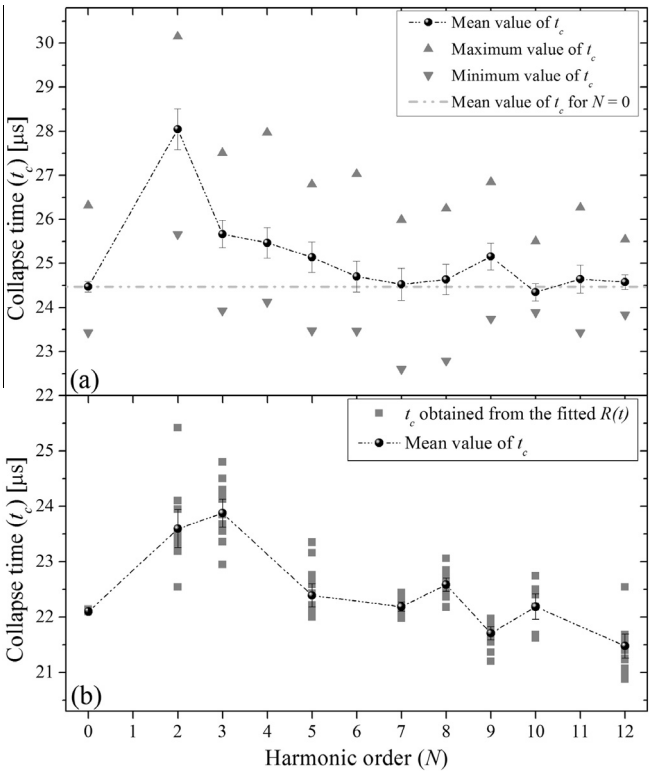

Fig. 16. Mean collapse time (t_c) as a function of the harmonic order (N) used in the bi-frequency driving. The data were taken applying two different experimental methods and using two distinct noble gases. The error bars represent the standard deviation of the data. (a) This experimental data was taken using xenon gas with a concentration of $c_\infty/c_0 \sim 12.10^{-3}$ dissolved in the SA. The experimental data is the average of seven traces taken during pressure ramps (as shown in Fig. 15) setting different values of α with 60° of separation in each measurement. In all cases we used a driving frequency of $f_0 = 29$ kHz and similar values of V_{PZT}^{HF} (just below the cavitation threshold). The error bars indicate the mean standard deviation of the data. (b) Collapse time of argon bubbles obtained from the numerical fits of the series of $R(t)$ measured under random conditions for different values of N (see Fig. 2). The mean c_∞/c_0 was $\sim 12.10^{-3}$.

shown how the mean value of the collapse time was greater for the lower harmonics and tended progressively to the value obtained with single frequency driving as N was increased, being this in agreement with the simulation described in Fig. 11 and the experimental results reported in Fig. 5 of Ref. [19].

4. Conclusions

In this work, we performed an extensive parametric study in order to achieve a deeper understanding about the role of the high frequency component of the acoustic field in the dynamics of sonoluminescent bubbles driven with bi-harmonic signals in H_2SO_4, specifically in a Ar–SA85 or Xe–SA85 systems.

The diversity of data gathered during this research, consisting of both experimental results and numerical simulations, let us analyze the phenomenon under discussion from a general perspective. This kind of study allowed us to further understand not only the many advantages of the use of multi-harmonic driving in Sonoluminescence, but also some unexplored corners of the bubble dynamics itself like the absence of sharp resonances peaks in the expansion ratio (observed in Fig. 1(b)), for typical acoustic pressures used in Sonoluminescence in the case of SA85, in contrast to that reported in water based systems.

Regarding to the positional instability, a numerical study of the physical parameters achieved by bubbles at equilibrium was carried out for cases using harmonic frequencies (Nf_0) ranging from $N = 2$ to $N = 15$. These simulations were related to three prototypical situation ((1)–(3)) classified according to the pressure amplitude of P_{Ac}^{LF} and P_{Ac}^{HF} in the resonator center. As shown in Fig. 7, for scenarios (1) and (2) the bubbles settled in different equilibrium positions r_{eq} away from the main antinode depending on which harmonic frequency component (Nf_0) was added to P_{Ac}^{LF}, while for the remaining scenario (3) both components of $\vec{F}_b$ are attractive to the antinode for all N. In (1) and (2) the bubbles got closer to $r = 0$ for higher values of N. Consequently, the use of high frequencies driving improves the positional stability compared to cases with low order harmonics (e.g. $N = 2, 3$). When the bubbles were already stabilized over the pressure antinode as in (3), the changes in their radial dynamics were independent of the specific pressure profile generated by the particular mode being excited. Still for those cases, the simulated results displayed in Fig. 8 show a convergence of all the analyzed parameters towards the ones obtained with single frequency driving ($N = 0$) as the harmonic order was increased.

A variation in φ_b changed the bubble dynamics in relevant aspects like the spatial stability, the equilibrium position and the light intensity emitted by the bubble. Moreover, the existence of regions of the R_0—φ_b parameter space where the bubbles can not "survive" due to the shape or positional instabilities, was demonstrated experimentally in Fig. 3 and also through calculus in Figs. 5, 6 and 10. Regarding to the positional stability, the effect of the relative phase on the behavior of the bubbles decreases significantly according N increases (see Figs. 11, 14 and 16).

The presence of P_{Ac}^{HF} in the acoustic pressure field inhibited the bubble dissolution with respect to the case with single frequency driving, while additionally promoted the generation of multiple bubbles by acoustic cavitation.

On the other hand, the effect of the HF component on the bubble radial dynamics was also examined experimentally. Initially, the shape of several measured traces of the $R(t)$ was analyzed. A remarkable resemblance between the $R(t)$ taken with $N = 0$ and the ones measured with biharmonic driving, was observed as harmonic order N was increased (Fig. 3).

The parametric analysis of the experimental data confirmed all the conclusions derived from the numerical simulations. Furthermore, the multivariate analysis pointed out the existence of many dependencies among the characteristic parameters involved in the dynamics of SL bubbles. In particular, the correlation found between t_c and some important bubble parameters like R_{max}/R_0, φ_b and P_{Ac}^{LF} revealed that the collapse time is a proper parameter to characterize SL systems. All the experimental results gathered in this work, composed by numerical fits of numerous $R(t)$ and direct measurements of the collapse time of argon and xenon bubbles indicated that, regardless of the bubble position or the concentration of gas dissolved in the liquid, the HF component of the acoustic field has a relevant impact on the SL bubbles, only by reducing the effect of the spatial instability as its frequency moves away from the fundamental.

This research has shown that each frequency component of a biharmonic acoustic field can be used in an uncoupled fashion to produce different effects on the SL bubbles. For example, P_{Ac}^{LF} can be used to regulate the diffusive, positional and shape stability, while suppressing the spatial stability (reducing the pseudo-orbits) through P_{Ac}^{HF}, by setting harmonics with $N \gg 1$. On the other hand, controlling φ_b may be a useful experimental technique to confine the bubble (handling $|\vec{F}_b|$ to be attractive) when low order harmonics are used (e.g. $N = 2, 3$). Moreover, this could be useful to increase the maximum temperature reached by the bubble in its collapse.

Acknowledgement

We gratefully acknowledge Sonia Esquivel Mattos for the English revision of the manuscript. J.M.R. was supported with a postdoctoral scholarship granted by CONICET.

References

[1] T.J. Matula, Bubble levitation and translation under single-bubble sonoluminescence conditions, J. Acoust. Soc. Am. 114 (2) (2003) 775–777.
[2] D.F. Gaitan, A. Crum, C. Church, A. Roy, Sonoluminescence and bubble dynamics for a single, stable, cavitation bubble, J. Acoust. Soc. Am. 91 (6) (1992) 3166.
[3] J. Holzfuss, M. Rüggeberg, R. Mettin, Boosting sonoluminescence, Phys. Rev. Lett. 81 (9) (1998) 1961–1964.
[4] F.B. Seeley, Effects of higher-order modes and harmonics in single-bubble sonoluminescence, J. Acoust. Soc. Am. 105 (4) (1999) 2236–2242.
[5] J. Ketterling, R. Apfel, Using phase space diagrams to interpret multiple frequency drive sonoluminescence, J. Acoust. Soc. Am. 107 (2) (2000) 819–826.
[6] K. Hargreaves, T. Matula, The radial motion of a sonoluminescence bubble driven with multiple harmonics, J. Acoust. Soc. Am. 107 (3) (2000) 1774–1776.
[7] F. Moraga, R. Taleyarkhan, R. Lahey, F. Bonetto, Role of very-high-frequency excitation in single-bubble sonoluminescence, Phys. Rev. E 62 (2 Pt A) (2000) 2233–2237.
[8] D. Krefting, R. Mettin, W. Lauterborn, Two-frequency driven single-bubble sonoluminescence, J. Acoust. Soc. Am. 112 (5) (2002). 1918-10.
[9] X. Lu, A. Prosperetti, R. Toegel, D. Lohse, Harmonic enhancement of single-bubble sonoluminescence, Phys. Rev. E 67 (5) (2003) 056310.
[10] S. Li, W. Chen, L. Jiang, Y. Zhu, C. Wang, Single bubble sonoluminescence driven by biharmonic ultrasound, Chin. Phys. Lett. 20 (11) (2003) 2053–2055.
[11] R. Urteaga, F.J. Bonetto, Trapping an intensely bright, stable sonoluminescing bubble, Phys. Rev. Lett. 100 (2008) 074302.
[12] R.E. Apfel, The role of impurities in cavitation-threshold determination, J. Acoust. Soc. Am. 48 (5) (1970) 1179–1186.
[13] J. Ketterling, R. Apfel, Shape and extinction thresholds in sonoluminescence parameter space, J. Acoust. Soc. Am. 107 (3) (2000) L13–L18.
[14] R. Urteaga, D. Dellavale, G. Puente, F.J. Bonetto, Experimental study of transient paths to the extinction in sonoluminescence, J. Acoust. Soc. Am. 124 (3) (2008) 1490.
[15] N.D. Flannigan, K. Suslick, Plasma formation and temperature measurement during single-bubble cavitation, Nature (London) 434 (2005) 52–55.
[16] S.D. Hopkins, S.J. Putterman, B.A. Kappus, K.S. Suslick, C.G. Camara, Dynamics of a sonoluminescing bubble in sulfuric acid, Phys. Rev. Lett. 95 (2005) 254301.
[17] A. Troia, D. Madonna Ripa, R. Spagnolo, Moving single bubble sonoluminescence in phosphoric acid and sulphuric acid solutions, Ultrason. Sonochem. 13 (2006) 278–282.
[18] R. Toegel, S. Luther, D. Lohse, Viscosity destabilizes sonoluminescing bubbles, Phys. Rev. Lett. 96 (11) (2006) 114301.

[19] D. Dellavale, L. Rechiman, J.M. Rosselló, F. Bonetto, Upscaling energy concentration in multifrequency single-bubble sonoluminescence with strongly degassed sulfuric acid, Phys. Rev. E 86 (2012) 016320.
[20] L.M. Rechiman, D. Dellavale, F.J. Bonetto, Path suppression of strongly collapsing bubbles at finite and low Reynolds numbers, Phys. Rev. E 87 (2013) 063004.
[21] J.M. Rosselló, D. Dellavale, F.J. Bonetto, Energy concentration and positional stability of sonoluminescent bubbles in sulfuric acid for different static pressures, Phys. Rev. E 88 (2013) 033026.
[22] J.M. Rosselló, D. Dellavale, F.J. Bonetto, Stable tridimensional bubble clusters in multi-bubble sonoluminescence (MBSL), Ultrason. Sonochem. 22 (2015) 59–69.
[23] I. Akhatov, R. Mettin, C. Ohl, U. Parlitz, W. Lauterborn, Bjerknes force threshold for stable single bubble sonoluminescence, Phys. Rev. E 55 (1997) 3747–3750.
[24] R. Urteaga, D.H. Dellavale, G.F. Puente, F.J. Bonetto, Positional stability as the light emission limit in sonoluminescence with sulfuric acid, Phys. Rev. E 76 (2007) 056317.
[25] J. Holzfuss, M. Rüggeberg, Acoustical stability of a sonoluminescing bubble, Phys. Rev. E 66 (4) (2002) 046630.
[26] D. Dellavale, M.O. Sonnaillon, F.J. Bonetto, FPGA based multi-harmonic control system for single bubble sonoluminescence, in: 4th Southern Conference on Programmable Logic, IEEE, Piscataway, NJ, 2008, p. 269.
[27] D. Dellavale, Algoritmos para el procesamiento concurrente de señales y su aplicación en sonoluminiscencia (Ph.D. Thesis), Instituto Balseiro, 2011.
[28] R.G. Holt, L.A. Crum, Mie scattering used to determine spherical bubble oscillations, Appl. Opt. 29 (1990) 4182.
[29] G.F. Puente, Sonoluminiscencia y cavitación en burbujas: análisis dinámico y de estabilidad en regiones altamente no lineales (Ph.D. Thesis), Instituto Balseiro, 2005;
G.F. Puente, R. Urteaga, F.J. Bonetto, Numerical and experimental study of dissociation in an air–water single-bubble sonoluminescence system, Phys. Rev. E 72 (2005) 046305;
G.F. Puente, P. García-Martínez, F.J. Bonetto, Single-bubble sonoluminescence in sulfuric acid and water: bubble dynamics, stability, and continuous spectra, Phys. Rev. E 75 (2007) 016314.
[30] R. Toegel, B. Gompf, R. Pecha, D. Lohse, Does water vapor prevent upscaling sonoluminescence?, Phys Rev. Lett. 85 (15) (2006) 3165.
[31] H. Lin, B.D. Storey, A.J. Szeri, Inertially driven inhomogeneities in violently collapsing bubbles: the validity of the Rayleigh–Plesset equation, J. Fluid Mech. 452 (2002) 145–162.
[32] V. Kellogg, International critical tables, Science 65 (1681) (1927) 273.
[33] D.R. Lide, CRC Handbook of Chemistry and Physics, ninetieth ed., CRC Press/Taylor and Francis, 2010.
[34] G. Schwab, E. Kolb, Zur viskositt der schwefelsure, Zeit. Phys. Chem. 3 (1) (1955) 52–64.
[35] N.F.H. Bright, H. Hutchison, D. Smith, The viscosity and density of sulphuric acid and oleum, J. Soc. Chem. Ind. 65 (12) (1946) 385388.
[36] D. Vray, D. Berchouz, P. Delachartre, G. Gimenez, Speed of sound in sulfuric acid solution: application to density measurement, Ultrasonics Symposium, Proceedings, vol. 2, IEEE, 1992, p. 969972.
[37] E. Abel, The vapor phase above the system sulfuric acidwater, J. Phys. Chem. 50 (3) (1946) 260–283.
[38] P. Koch, T. Kurz, U. Parlitz, W. Lauterborn, Bubble dynamics in a standing sound field: the bubble habitat, J. Acoust. Soc. Am. 130 (5) (2011) 3370–3378.
[39] M. Strasberg, Onset of ultrasonic cavitation in tap water, J. Acoust. Soc. Am. 31 (2) (1959) 163–176.
[40] M. Greenspan, C.E. Tschiegg, Radiation-induced acoustic cavitation; apparatus and some results, J. Res. Natl. Bur. Stand. 71C (1967) 299–312;
M. Greenspan, C.E. Tschiegg, Radiation-induced acoustic cavitation threshold versus temperature for some liquids, J. Acoust. Soc. Am. 72 (4) (1982) 1327–1331.
[41] S. Hilgenfeldt, D. Lohse, Predictions for upscaling sonoluminescence, Phys. Rev. Lett. 82 (5) (1999) 10361039.
[42] W. Lauterborn, T. Kurz, Physics of bubble oscillations, Rep. Prog. Phys. 73 (2010) 106501.
[43] R. Mettin, A.A. Doinikov, Translational instability of a spherical bubble in a standing ultrasound wave, Appl. Acoust. 70 (2009) 1330–1339.
[44] R.G. Holt, D.F. Gaitan, Observation of stability boundaries in the parameter space of single bubble sonoluminescence, Phys. Rev. Lett. 77 (18) (1996) 3791–3794.
[45] D. Dellavale, R. Urteaga, F. Bonetto, Analytical study of the acoustic field in a spherical resonator for single bubble sonoluminescence, J. Acoust. Soc. Am. 127 (1) (2010) 186–197.
[46] J.M. Rosselló, Frontera de estabilidad en sonoluminiscencia y concentración de energía en cavitación transitoria forzada (Ph.D. Thesis), Instituto Balseiro, 2015.
[47] A.J. Izenman, Multivariate Statistical Techniques. Regression, Classification, and Manifold Learning, Springer, 2008.